

AN EVALUATION OF A
THIN FILM X-RAY IMAGING SENSOR WITH LASER READ-OUT

AN EVALUATION OF A
THIN FILM X-RAY IMAGING SENSOR WITH LASER READ-OUT

By:

WILLIAM H.L. WAN, B.Sc.

A Project Report

Submitted to the School of Graduate Studies

in Partial Fulfilment of the Requirements

for the Degree of

Master of Engineering

[Part A]

McMaster University

Sept., 1986

MASTER OF ENGINEERING
(Engineering Physics)

TITLE: An Evaluation of a
 Thin Film X-ray Imaging Sensor
 With Laser Read-out

AUTHOR: Willian H.L. Wan, B.Sc.(University of Waterloo)

SUPERVISOR: Dr. N. Ramanathan*
 (Radiology Department, Toronto Western Hosiptal)

NUMBER OF PAGES: viii,69

* Formerly with Picker International Canada, Inc.

ABSTRACT

This report describes the industrial research work done during the summer of 1986. The main objective of this research was to develop a high resolution X-ray imaging system for mammographic applications. The basic set up of such system is quite simple: it consists of an X-ray tube; an X-ray sensor (which is coupled to the read out electronics), and the optical scanner assembly which serves as the reading device. Based on the feasibility studies carried out two years ago, much of the work during the past summer was targetted to improve the existing prototype, and to test out the new X-ray sensors. A new optical assembly was built for this system, which was used to examine the optical resolution of the new sensors. Experimental results were analysed using calculations of the resolution (MTF) of the sensors, and the results indicate that the latest sensors are capable of resolving a 1 mm diameter object. Unfortunately, due to the limitation of time, no X-ray exposure test were done on test targets. However, a theoretical model describing the X-ray sensors responses to X-ray radiation and laser light (based on previous work carried out by A. Zermeno et al, 1979) is presented here. Also, the results of the research work, carried out since the feasibility study up until the end of the summer of 1986, indicate that the sensors have a great potential for achieving limiting resolutions in the range of "0.1 mm" objects.

ACKNOWLEDGEMENTS

I wish to thank my supervisor Dr. N. Ramanathan for his constant encouragement and guidance throughout this project. I would also like to thank the other two team members, Mr. Q. Nguyen and Mr. T. Khosla, for their contributions to this project, and Dr. O. Caparoletti and his team at O.R.F. for fabricating the sensors to our specifications.

I am also thankful to Dr. E. A. Ballik for his help in my study. Finally, I am grateful to the people in the Radiology Department of Toronto Western Hospital for their assistance in the completion of this report.

The Thin Film Mammography Project was financially supported by the National Research Council of Canada — Industrial Research Assistance Program (P.I.L.P.), and Picker International Canada, Incorporated.

TABLE OF CONTENTS

ABSTRACT	iii
ACKNOWLEDGEMENTS	iv
LIST OF FIGURES	vi
LIST OF TABLES	vii
CHAPTER 1 INTRODUCTION	1
CHAPTER 2 BASIC DESCRIPTION OF THE IMAGING SYSTEM	6
2.1 Sensor	8
2.2 Optical Assembly	11
2.3 Electronics Data Acquisition System	15
CHAPTER 3 OPTICAL ASSEMBLY OF THE SYSTEM	17
3.1 Basic Design Criteria	17
3.2 Major Considerations	19
3.3 The Assembly	22
CHAPTER 4 SENSOR ENERGETICS	28
CHAPTER 5 EXPERIMENTAL RESULTS	34
CHAPTER 6 DATA ANALYSIS	39
6.1 MTF Definition	39
6.2 MTF Calculations	44
6.3 Analysis	45
CHAPTER 7 CONCLUSIONS AND RECOMMENDATIONS	56
REFERENCES	59
APPENDIX I	
- RAW DATA	60

LIST OF FIGURES

Figure	1.1	The Basic Concepts of the Imaging System	2
	1.2	Layout of the Sensor	4
	2.1	The Large Format Sensor X-ray Imaging System	7
	2.2	Structure of the X-ray Sensor	9
	2.3	Optical Assembly of the Imaging System	12
	2.4	Laser Spot Position on the Sensor at different times of the scan	14
	2.5	Electronics of the Imaging System	16
	3.1	A Horizontal Straight Line Scan	18
	3.2a)	Basic Structure of a Laser Cavity	20
	b)	Focussing of a Laser Beam by a Focussing lens	20
	3.3a)	Divergence of a Laser Beam	23
	b)	Laser Beam Expander	23
	3.4	Layout of of the Optical Assembly	25
	3.5	Geometry of a Scan	27
	4.1	Structure of the Sensor as a Parallel Plate Capacitor	29
	4.2	Percentage Absorption vs KVP of X-ray	33
	5.1a)	Typical Optical Waveform	35
	b)	Ideal Waveform	35
	c)	Response Function of the Sensor	35
	6.1	Optical Waveform of Sensor #1126B	40
	6.2	Input Function	41
	6.3	Response Function of Sensor #1126B	42
	6.4	MTF vs s for Sensor #1126B at Scanspeed 128 lines/sec	46
	6.5	MTF vs s for Sensor #1126B at Scanspeed 256 lines/sec	47

6.6	MTF vs s for Sensor #1126B at Scanspeed 512 lines/sec	48
6.7	MTF vs s for Sensor #1114B at Scanspeed 128 lines/sec	49
6.8	MTF vs s for Sensor #1114B at Scanspeed 256 lines/sec	50
6.9	MTF vs s for Sensor #1114B at Scanspeed 512 lines/sec	51
6.10	MTF vs s for Sensor #870A at Scanspeed 128 lines/sec	52
6.11	MTF vs s for Sensor #870A at Scanspeed 256 lines/sec	53
6.12	MTF vs s for Sensor #870A at Scanspeed 512 lines/sec	54

LIST OF TABLES

Table. II.1	Thickness of PbO and SiO of Sensor #870A, #1114B and #1126B	10
V.1	Amplitudes, rise and fall constants of each Sensor at Scanspeed 128, 256 and 512 lines/sec	38
VI.1	Limiting resolution of Sensor #870A, #1114B and #1126B at Scanspeed 128, 256 and 512 lines/sec	55

CHAPTER 1

INTRODUCTION

The main objective of this Thin Film Mammography Project is to develop a high resolution X-ray imaging system. One major application of X-ray mammography is the early detection and diagnosis of breast cancer. An early warning sign showing the development of breast cancer is the identification of minute calcium deposits in the breast [1]. These calcium particles are usually 0.1 to 1.0 mm in diameter. The capability to detect and identify such "microcalicification" is a key to successful early diagnosis of breast cancer, and this is what the high resolution X-ray imaging system would have to accomplish.

This research project was undertaken by the Engineering Research Group of Picker International Canada, Inc. The research group was headed by Dr. N.Ramanathan, with Mr. Q.Nguyen, Mr. T.Khosla and the author as members of the research team. The imaging system employs, instead of the conventional X-ray screen/film, a thin film of semiconductor material deposited on a glass substrate, as the X-ray sensor (it is fabricated at the Ontario Research Foundation by Dr. O. Caparoletti according to specification provided by Picker). The basic idea of the imaging system is shown in Fig. 1.1. The image of the object, impressed on the sensor by X-ray radiation, is read off by a laser flying-spot scan [1,2]. During the scan, a photocurrent is produced by the sensor due to the incident laser light. The amplitude of this photocurrent signal depends on the amount of X-ray radiation

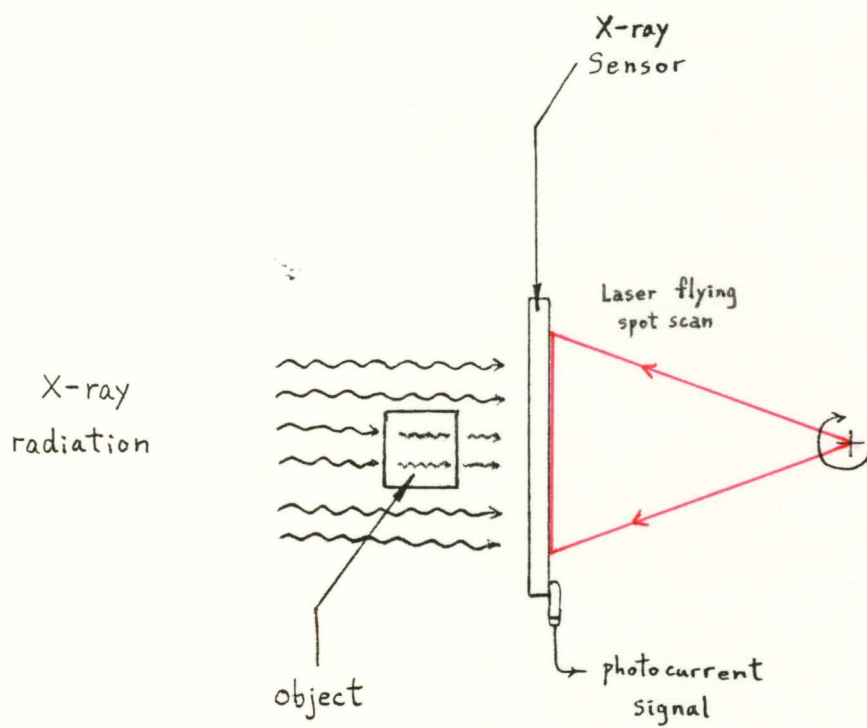
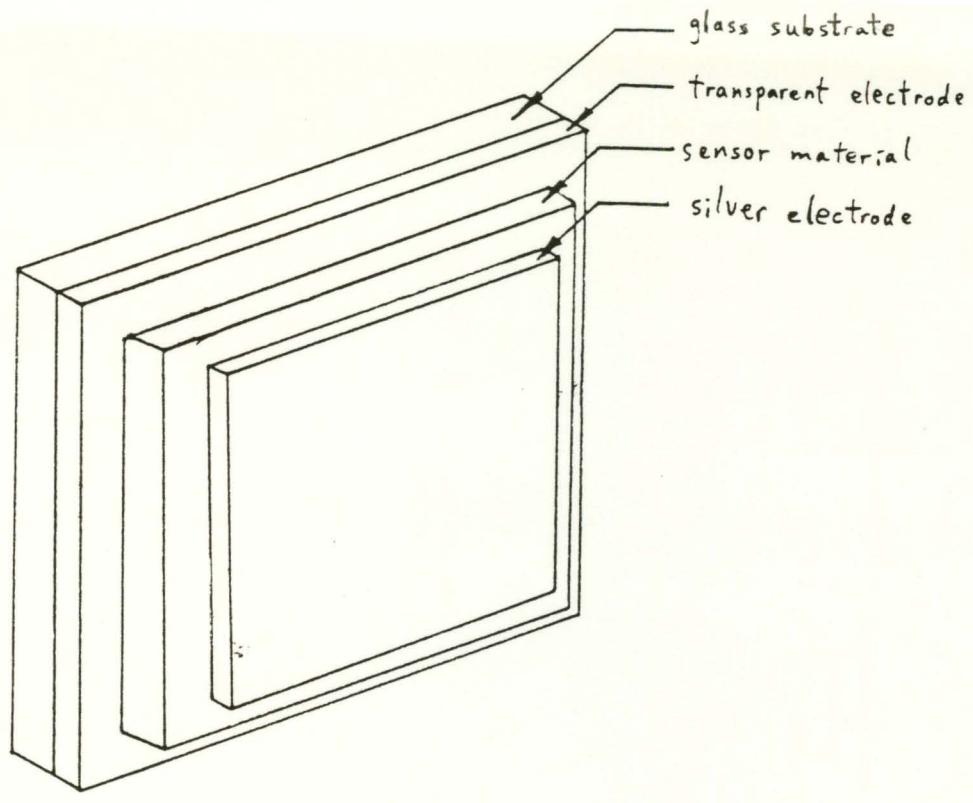


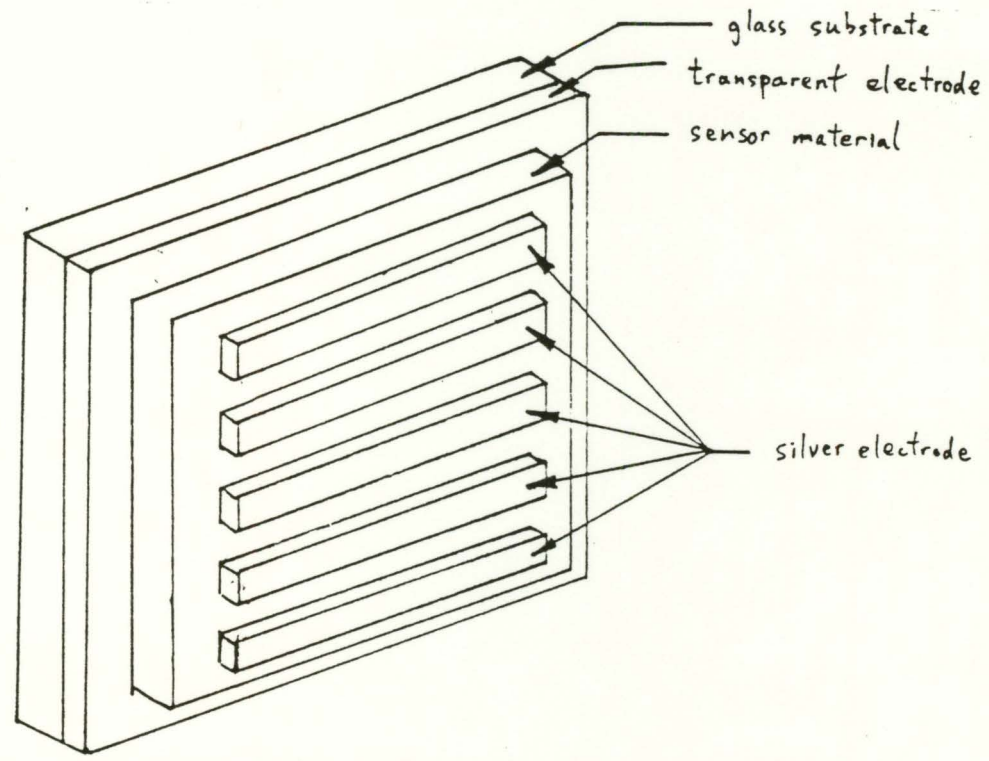
Figure 1.1 The Basic Concepts of The Imaging System

incident on the sensor. The photocurrent signal can be digitized easily and stored numerically in a computer. Then, using the basic parameters of the imaging system, the image of the object can be reconstructed. Note that unlike the conventional X-ray screen/film, the X-ray sensor is reusable. Also, the image can be developed by the computer, which is much faster than the conventional process. Due to the new approach in X-ray imaging, the understanding of the X-ray sensor response to X-ray radiation and laser light (i.e. the solid-state physics of the sensor) becomes an integral and key part of the research program.

During the period from 1983 to 1984, a feasibility study for the research program was carried out, a simple working model (prototype) was built and preliminary experiments were conducted. Results had shown that the program was definitely worthwhile of pursuing [1,2]. In the beginning of May, 1986, when this project was started, the prototype was brought back to working condition. The emphasis of the work, during the summer of 1986, was to improve the prototype (design a new optical assembly: carried out by the author), and to design a new data acquisition system (carried out by Mr. Q. Nguyen and Mr. T. Khosla). In addition, studies were carried out on the response of the sensor to X-ray radiation and HeNe red laser light. Three sets of sensors were tested; 1) sensor #870A (used in the prototype built in 1983), 2) sensor #1114B (fabricated at the beginning of the summer, 1986) and 3) sensor #1126B (the most recently fabricated). A multiple-strip layout was employed for the two new sensors, instead of the areal layout used for sensor #870A, see Fig. 1.2.



a) areal layout (sensor #870A)



b) multiple-strip layout (sensors #1114B, #1126B)

Figure 1.2 Layout of The Sensors

In this report, a brief description of the system is presented in Chapter 2. A more detailed discussion concerning the optical assembly is given in Chapter 3. Currently, the response of the thin film sensor to X-ray radiation is not fully understood yet. However, a simple theoretical model for the sensor [7] presented in Chapter 4 will serve as a guide for the time being. The results and the analysis are presented in Chapters 5 and 6, respectively. Finally, conclusions and recommendations are made and presented in Chapter 7.

CHAPTER 2

BASIC DESCRIPTION OF THE IMAGING SYSTEM

The large format sensor X-ray imaging system can be broken down into several basic components, and they are the: i) X-ray tube, ii) sensor, iii) optical assembly, and iv) the electronics data acquisition system (Fig. 2.1).

The basic principles of how this imaging system works are: a) the X-ray tube produces the X-ray radiation for the exposure; b) after being attenuated by the target, the radiation will impress an "image" on the sensor; c) then, the optical scanner will read off the information by using a laser flying-spot scan across the sensor, which produces a photocurrent signal; d) finally, this current is converted into digital information for analysis and display. It should be noted that the X-ray exposure taken in this system (i.e., step 'a' and step 'b') are same as any other conventional system; the major difference is how the "picture" or "image" is being developed. In this system, a specially fabricated X-ray sensor, which is a thin film of semiconductor materials, is used in place of the conventional X-ray screen or film, and the image is processed using steps 'c' and 'd'.

This chapter will briefly describe each of the major components of the imaging system, except for the X-ray tube, which is the same as any other conventional system.

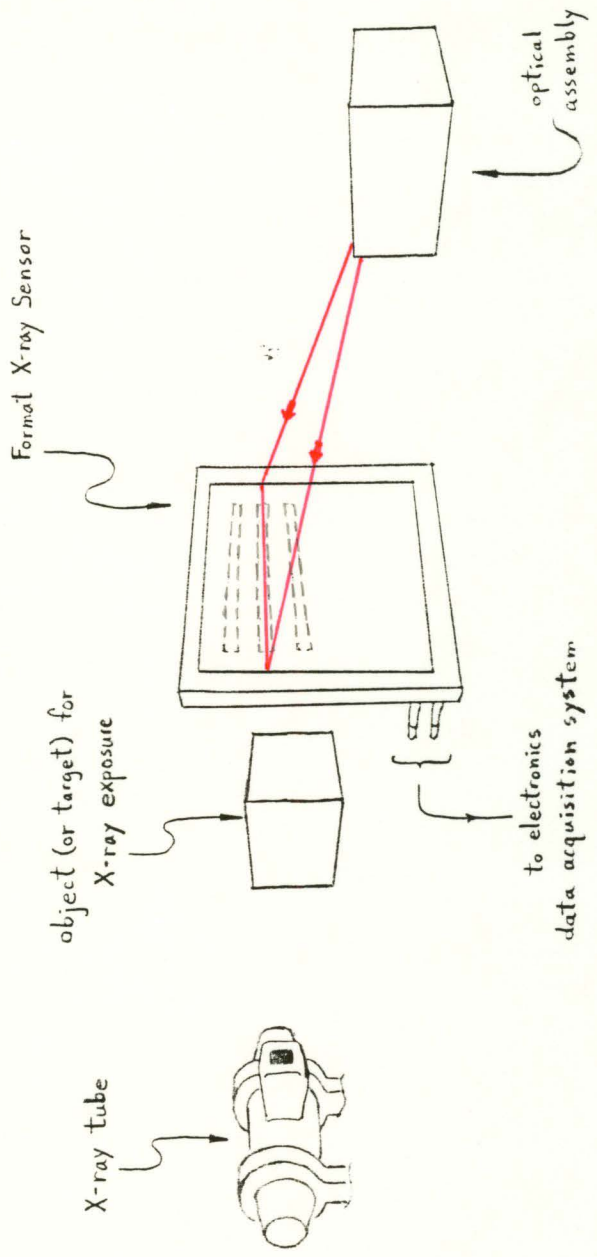


Figure. 2.1 The Large Format Sensor X-ray Imaging System

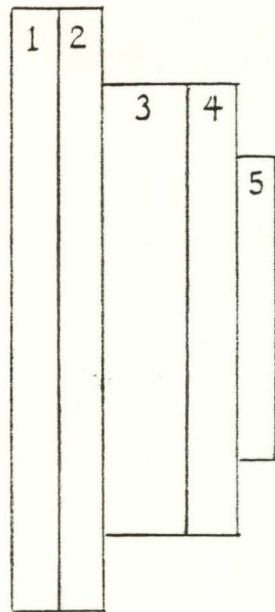
2.1 Sensor

The X-ray sensor is a sandwich structure of semiconductor materials (Fig. 2.2). The X-ray detector layer is made out of tetragonal PbO (lead monoxide), and the insulator is SiO (silicon monoxide). In this study, three different batches of sensors were tested. They are denoted as sensor #870A, #1114B, and #1126B. The basic structure of these sensors are the same, except that the thicknesses of PbO and SiO layers for each sensor are different (Table II.1).

PbO is chosen as the X-ray detector material because of its strong X-ray absorption coefficient [2], and its sensitivity to red light. From previous experiments, results had shown that the absorbed X-ray would induce charges on the PbO layer. When laser light is incident on the PbO, these induced charges would be dissipated as current (i_{X-ray}) with its amplitude proportional to the X-ray dose absorbed by the sensor. However, the PbO is also a photoconductor. Consequently, laser light will produce a photocurrent (i_{laser}) even in the absence of X-rays. Therefore, during a laser flying-spot scan across the sensor, the photocurrent is a combination of the current due to X-ray and the current due to laser light [2]. Experiments have shown that the photocurrent measured can be expressed as:

$$i_{meas} = i_{laser} - i_{X-ray} \quad (2.1)$$

Although the reason for this anomalous behaviour (difference of i_{laser} and i_{X-ray} rather than the sum) of Eq.(2.1) is still not known. However, the equation provides the basics information necessary to analyse the data and to extract the "image" out.



layer:

- 1 — glass substrate
- 2 — transparent electrode
- 3 — X-ray detector layer (PbO)
- 4 — insulating layer (SiO)
- 5 — silvered electrode

Figure 2.2 Structure of the X-ray Sensor

Sensor	Thickness of	
	PbO	SiO
#870A	80 μm	40 μm
#1114B	43 μm	27 μm
#1126B	43 μm	81 μm

Table II.1 Thickness of PbO and SiO of Sensor
#870A, #1114B and #1126B

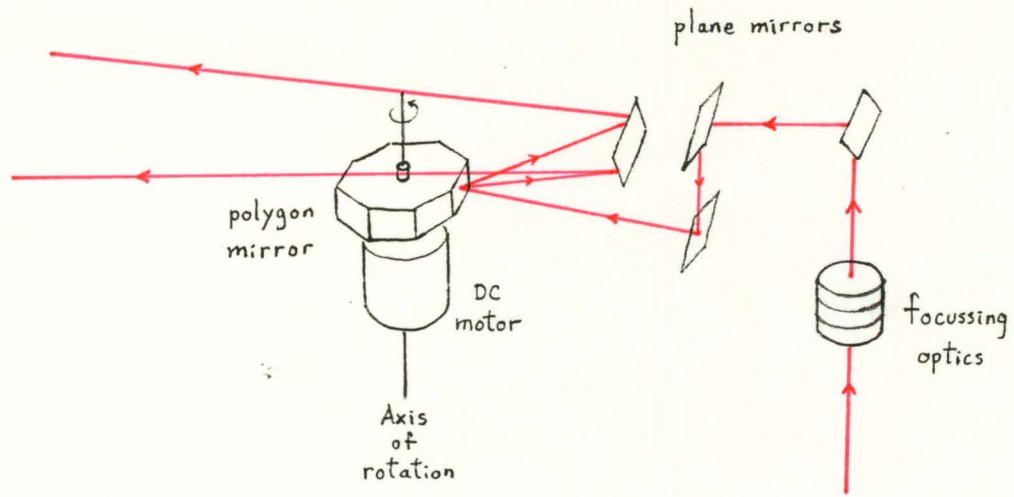
A more detailed discussion about the sensor energetics will be presented in Chapter 4.

2.2 Optical Assembly

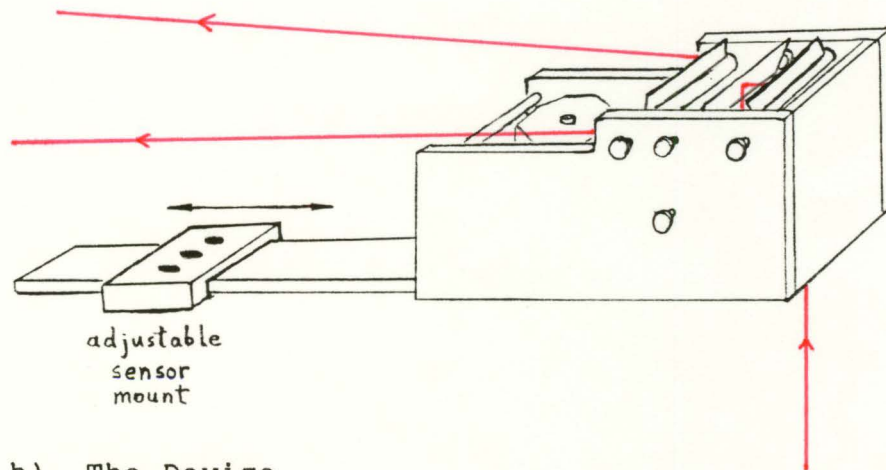
The optical assembly of the imaging system is basically a laser scanner, which is made up of a rotating polygon mirror, plane mirrors, focussing optics, and a laser source (Fig. 2.3). The assembly is used for reading the sensor by providing a laser flying-spot scan. As mentioned in section 2.1, the photocurrent, i_{meas} , produced due to incident laser light, also depends on the amount of X-ray absorbed by the sensor. Depending on the object, different locations on the sensor absorb different amounts of X-ray radiation and produce the latent "image" on the sensor. Therefore, as the laser spot scans across the sensor, the photocurrent varies according to the distribution of X-ray absorbed across the sensor. Because the laser spot takes a finite time to scan across the sensor, the measured signal is a function of time, i.e., $i_{\text{meas}} \equiv i_{\text{meas}}(t)$, corresponding to different locations on the sensor. Using the velocity of the laser spot on the sensor surface (v), $i_{\text{meas}}(t)$ can be transformed into $i_{\text{meas}}(x)$, where x is defined as the position on the sensor, and it is given by:

$$x = v \cdot t \quad . \quad (2.2)$$

In the present optical assembly, the scanner only provides a horizontal straight line scan, because the sensor has a multiple-strip layout. However, if desired, the scanner can be modified to provide vertical scan motion as well by using a stepping motor



a) General Concepts



b) The Device

Figure 2.3 Optical Assembly of the Imaging System

for the vertical motion. Then $i_{meas}(t)$ can be transformed into $i_{meas}(x,y)$, where x and y are defined as the horizontal and vertical positions on the sensor, given by:

$$x = v.(t-t_{n-1}) \quad , \quad (2.3)$$

$$y = \Delta y.(n-1) \quad . \quad (2.4)$$

for $t_{n-1} < t < t_n$,

and $n = 1,2,3,4,\dots$,

where v is velocity of the laser spot as it scans across the sensor. Δy is the increment of the laser spot position on the sensor in the vertical direction, due to the stepping motor, and (t_{n-1}, t_n) is the time interval during which the laser spot is on its n^{th} line scan (Fig. 2.4).

It can be assumed that i_{laser} is constant throughout the scan. Therefore, Eq.(2.1) can be rewritten as

$$i_{X-ray}(x) = i_{laser} - i_{meas}(x) \quad . \quad (2.5)$$

Since $i_{X-ray}(x)$ is proportional to the amount of X-ray absorbed at x , the "image" of the target can be reconstructed. A more detailed discussion concerning the optical assembly (i.e., its basic design criteria, major considerations and limitations) will be presented in Chapter 3.

2.3 Electronics Data Acquisition System

The data acquisition system, is made up of i) a current control "Noise Subtraction Scheme" amplifying circuit [3], ii) a digital storage oscilloscope (Tektronix model# 468), and iii) an X-Y plotter. Viewing the system electronically, the silvered

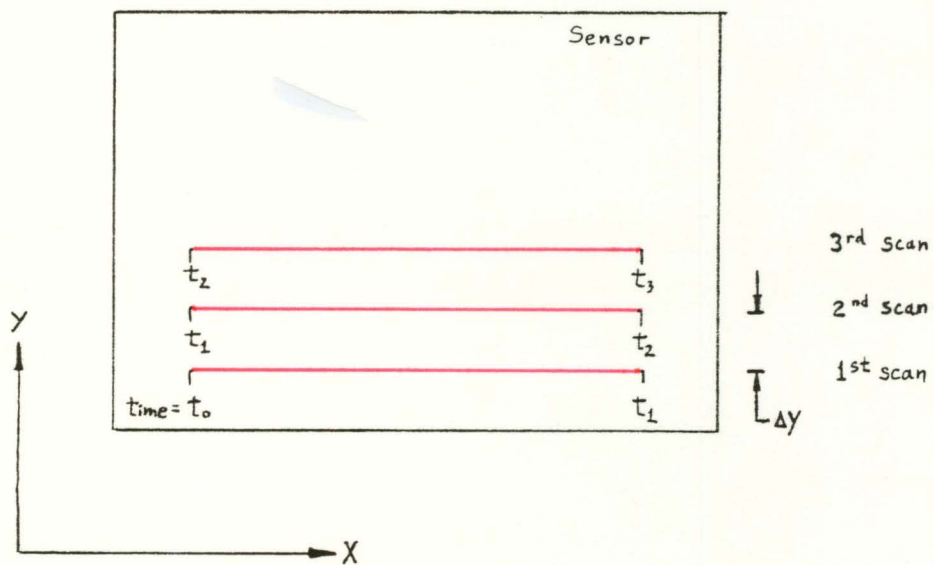


Figure 2.4 Laser Spot Position on the Sensor at different time of the scan

terminal of the sensor is connected to the input of the amplifying circuit, then the output of the amplifier is connected to the digital storage scope; on the other hand, the transparent terminal of the sensor is connected to the positive (+) terminal of a dc bias source, and from the negative (-) terminal of the dc bias, it is connected to the ground of the amplifying circuit (Fig. 2.5).

During a laser flying spot scan, a photocurrent signal will be generated as the spot passes through the sensor. This signal is first amplified by the "Noise Subtraction Scheme" amplifier. Then the amplified signal is collected and stored by the oscilloscope. A "hard copy" of this amplified signal can be obtained with the X-Y plotter.

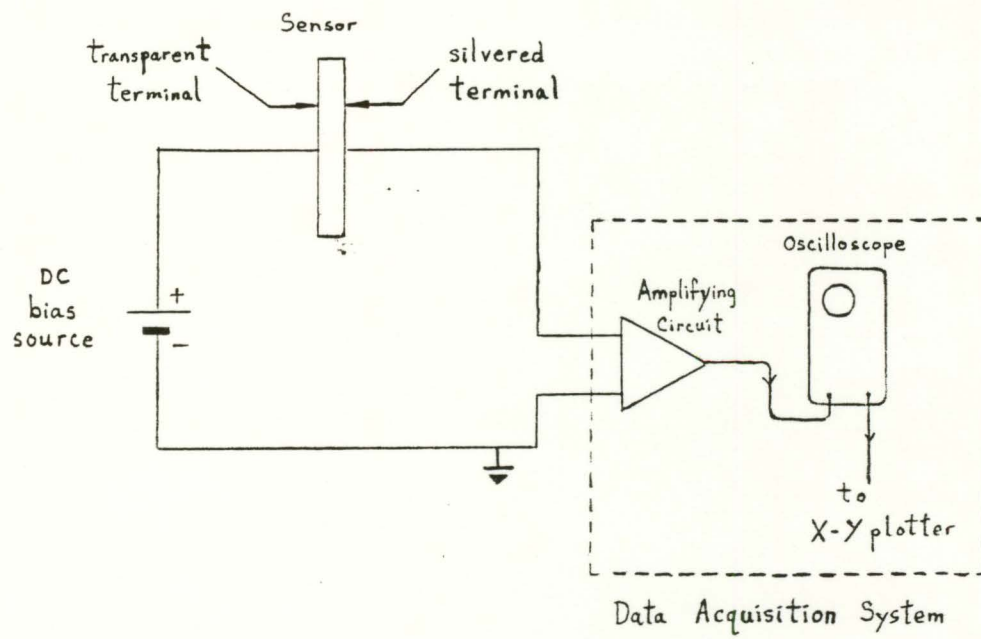


Figure 2.5 Electronics of the Imaging System

CHAPTER 3

OPTICAL ASSEMBLY OF THE SYSTEM

As discussed in section 2.2, the optical assembly serves to read the image on the sensor. It is basically a laser scanner consisting of several major components, including i) an 8-facet polygon mirror (with a dc motor drive)[†], ii) plane mirrors, iii) a red HeNe laser source and iv) focussing optics. During the feasibility study (1983 to 1984), a simple working model was used. However, for the actual development of the system, a more compact and carefully designed optical assembly is required; As a result, most of the work carried out during the summer of 1986, was improving the optical assembly. This chapter presents the basic design criteria, major limitations and considerations of the new assembly.

3.1 Basic Design Criteria

In the imaging system, the sensor layouts are in multiple-strip form (i.e., #1114B and #1126B). Requiring a straight line scan. Therefore, the new scanner has to provide a horizontal straight line scan covering a width of approximately 14 inches (or 36 cm) wide with a scan angle of $\pm 20^\circ$. The desirable spatial resolution is 2048 pixels/line; thus, requiring a laser spot diameter of approximately 100 μm (Fig. 3.1).

[†] — Lincoln Laser Company: Model #S-600-010-LVB0B

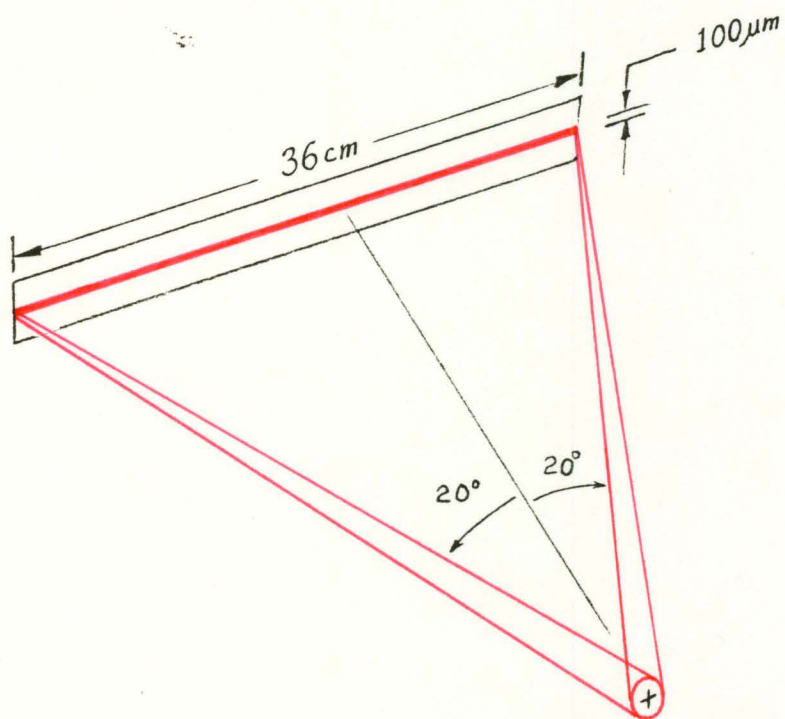


Figure 3.1 A Horizontal Straight Line Scan

3.2 Major Considerations for Scanner Design

The material used for the X-ray sensor is tetragonal PbO, chosen for its high X-ray absorption coefficient [2]. This material is also highly sensitive to visible red light. Therefore a HeNe red laser was used as the light source. Some principles of laser physics and geometrical optics should be considered, before discussing any further with the design. The laser employed was a Melles Griot HeNe laser, model #05LHP141, operating @ $\lambda = 6328\text{\AA}$, with 4 mW cw output power and a Gaussian irradiance profile (i.e. TEM₀₀ mode). Therefore, this section will assume Gaussian beam optics.

A TEM₀₀ mode laser output beam has a wavefront curvature and beam radius given by

$$R(z) = z \left[1 + \left(\frac{\pi W_0^2}{\lambda z} \right)^2 \right] \quad (3.1)$$

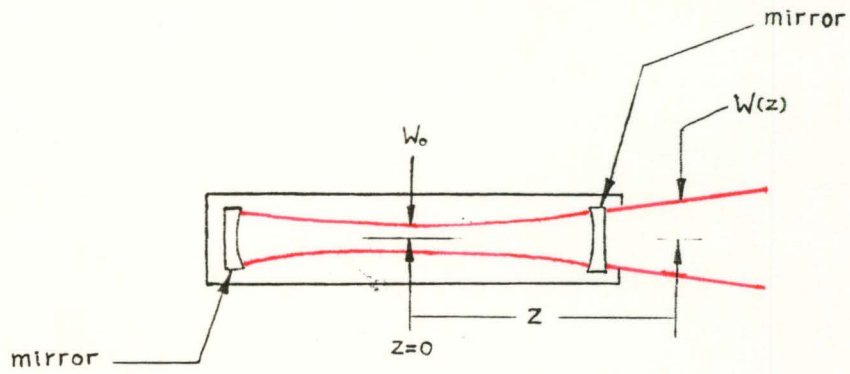
$$\text{and } W(z) = W_0 \left[1 + \left(\frac{\lambda z}{\pi W_0^2} \right)^2 \right]^{1/2}, \quad (3.2)$$

respectively [4,5]. Where λ is the laser wavelength, and W_0 is the minimum beam radius at $z = 0$ (Fig. 3.2).

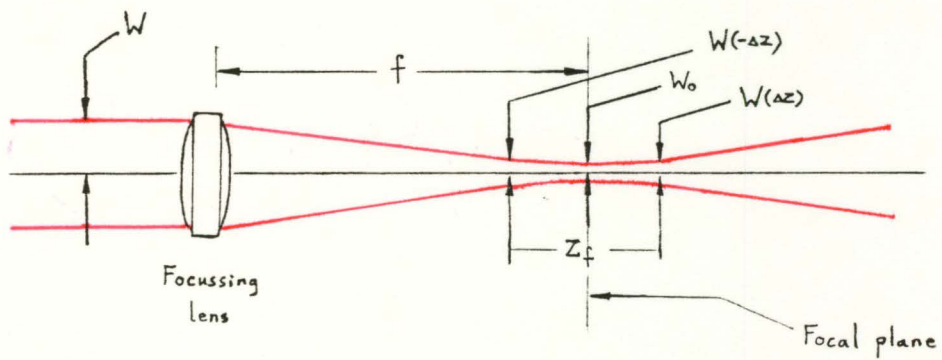
When focussing the laser beam with an aberration free lens (i.e. an achromats lens) the final minimum spot size is not zero, as simple geometrical optics might suggest, but it is given by

$$W_0 = \frac{\lambda f}{\pi W} \quad (3.3)$$

for $f \gg \frac{\pi W_0^2}{\lambda}$, where W is the original beam radius at the lens, f is the focal length of the lens, λ is the wavelength of the laser, and W_0 is the spot radius at the focal plane (Fig.3.2b). The depth of focus, Z_f , of a focussed beam is also a very useful



a) Basic Structure of a Laser Cavity



b) Focussing of a Laser beam by a Focussing Lens

Figure 3.2

parameter. It is defined as the range where the laser spot size remains minimal within some specified percentage (5% or 10%) of defocussing.

For example, let $Z_f = 2\Delta z$, in the 10% defocussing case.

Substitution of $W(\pm\Delta z) = 1.10W_0$ into equation (3.2) yields

$$\begin{aligned} W(\pm\Delta z) &= W_0 \left[1 + \left(\frac{\pm\Delta z \lambda}{\pi W_0^2} \right)^2 \right]^{1/2} \\ &= 1.10W_0, \end{aligned}$$

and,

$$\begin{aligned} 1.10W_0 &= W_0 \left[1 + \left(\frac{\pm\Delta z \lambda}{\pi W_0^2} \right)^2 \right]^{1/2} \\ 1.21 &= 1 + \frac{\Delta z^2 \lambda^2}{\pi^2 W_0^4} \\ 0.21 &= \frac{\Delta z^2 \lambda^2}{\pi^2 W_0^4} \\ \Delta z &= \frac{0.46\pi W_0^2}{\lambda} \end{aligned}$$

Therefore, the depth of focus for 10% defocussing is

$$Z_f = 2\Delta z = \frac{0.92\pi W_0^2}{\lambda}. \quad (3.4)$$

Similarly, for a 5% defocussing,

$$Z_f = \frac{0.64\pi W_0^2}{\lambda}. \quad (3.5)$$

Another limitation on the scanner performance is the divergence of the laser beam (Fig. 3.3a). The Melles Griot HeNe laser has an output beam diameter of 0.8 mm [6]. From the divergence equation given as

$$\theta = 0.637 \frac{\lambda}{D}, \quad (3.6)$$

where λ is the wavelength, and D is the aperture. The divergence angle θ is equal to 0.5 mrad. From simple geometry, a 1 m focal length lens will have a spot size of,

$$\begin{aligned} 2f\theta &= 2 (1000 \text{ mm}) (0.5 \times 10^{-3} \text{ rad}) \\ &= 1.0 \text{ mm} \end{aligned}$$

1.0 mm in diameter. Therefore, in order to focus the laser beam

down to a spot size of 100 μm (see section 3.3), the original beam must be expanded first. From Eq.(3.6), it can be seen that the beam divergence is inversely proportional to the beam diameter (or aperture).

The purpose of a laser beam expander is to expand a collimated beam of diameter d_1 to a collimated beam of diameter d_2 . The simplest setup of a beam expander is to have two simple focussing lenses and place them along the same optical axis with their focal planes coincide with each other (Fig. 3.3b). The expansion ratio is given as

$$d_1:d_2 = f_1:f_2, \quad (3.7)$$

where f_1 and f_2 are the focal lengths of lens 1 and lens 2, respectively.

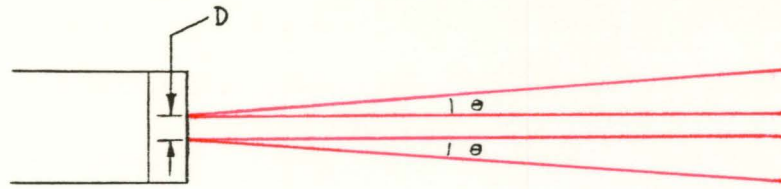
3.3 The Assembly

A Melles Griot 10X beam expander (model #09LBM003) is adopted to the HeNe laser providing an 8 mm diameter output beam. From Eq.(3.6),

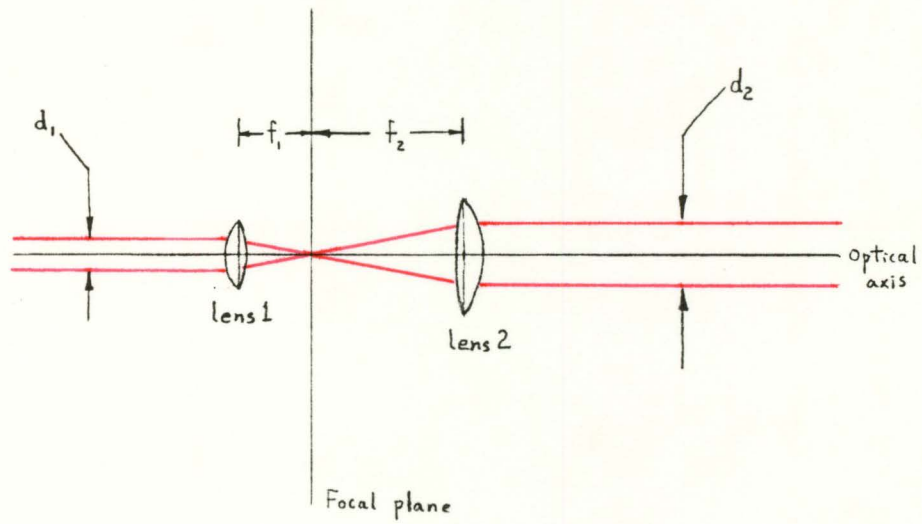
$$\begin{aligned} \theta &= 0.637 \frac{\lambda}{D} \\ &= 0.637 \left(\frac{6328 \text{ \AA}}{8 \text{ mm}^{-3}} \right) \\ &= 0.0504 \times 10^{-3} \text{ rad} \end{aligned}$$

which gives a divergence angle of ~ 0.05 mrad (a reduction of 10X in beam divergence). An achromats lens of focal length $f = 1.0$ m is used as the focussing lens. From Eq.(3.3),

$$\begin{aligned} W_0 &= \frac{\lambda f}{\pi W} \\ &= \frac{(6328 \text{ \AA})(1.0 \text{ m})}{\pi(4.0 \text{ mm})} \end{aligned}$$



a) Divergence of the Laser Beam



b) Laser Beam Expander

Figure 3.3

$$W_0 = 50.36 \mu\text{m}$$

$$2W_0 = 100.7 \mu\text{m}$$

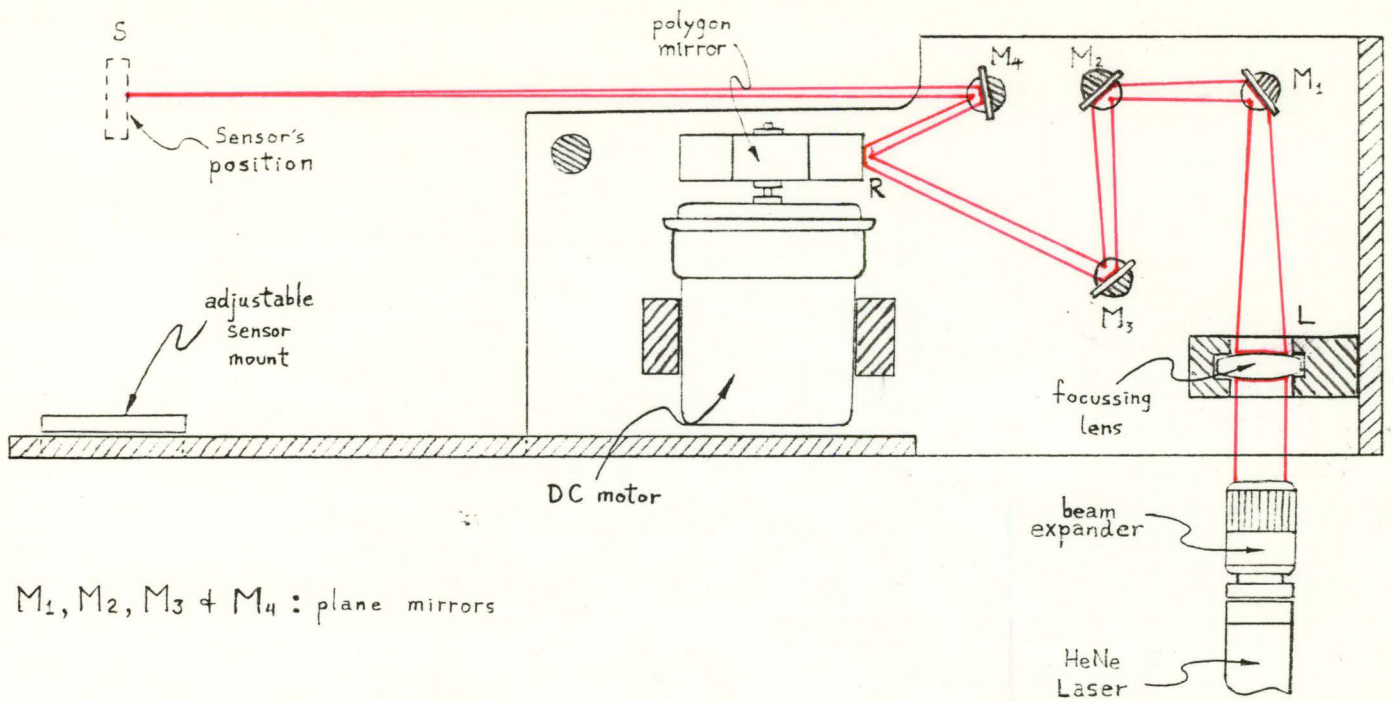
This yields a spot diameter of approximately 101 μm . Substitute W_0 into Eqs.(3.4) or (3.5) gives,

$$\begin{aligned} Z_f &= \frac{0.92\pi W_0^2}{\lambda} && \text{(for 10\% defocussing)} \\ &= \frac{0.92\pi (50.36 \mu\text{m})^2}{(6328 \text{ \AA})} \\ &= 11.6 \text{ mm} \end{aligned}$$

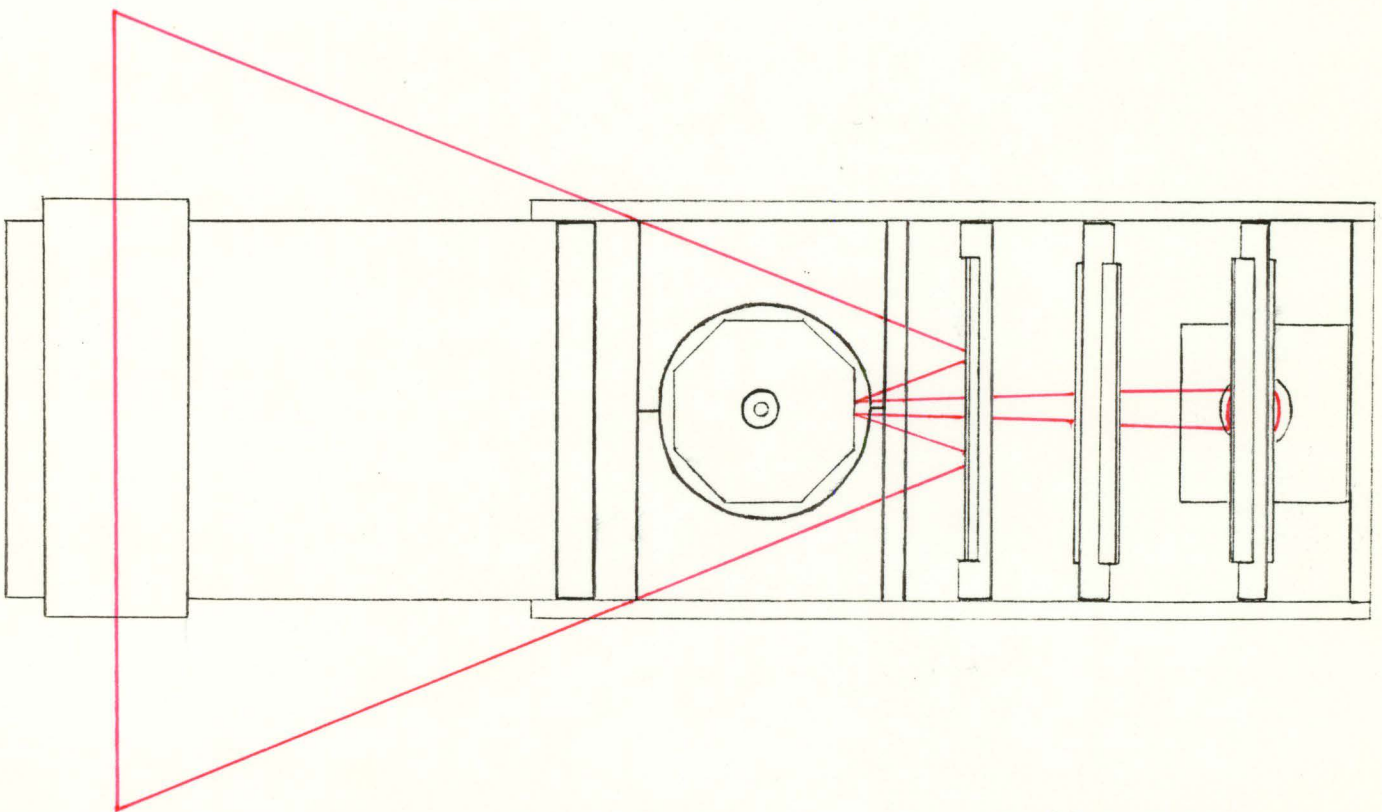
$$\begin{aligned} \text{or } Z_f &= \frac{0.64\pi W_0^2}{\lambda} && \text{(for 5\% defocussing)} \\ &= 8.1 \text{ mm} \end{aligned}$$

The depth of focus is 11.6 mm or 8.1 mm for a 10% defocussing or a 5% defocussing, respectively.

The general design concept is quite simple. The laser light from the HeNe laser is first expanded, and then focussed back down to a spot size of $\sim 100 \mu\text{m}$ in diameter, using a 1.0 m focal length lens. Immediately after the focussing lens, plane mirrors are used for redirecting the converging beam to the rotating polygon mirror, which provides the actual laser flying-spot scan. A layout of this optical assembly is shown in Fig. 3.4. The distance from the focussing lens to the sensor (i.e., $L \rightarrow M_1 \rightarrow M_2 \rightarrow M_3 \rightarrow R \rightarrow M_4 \rightarrow S$) is set equal to the focal length of the focussing lens (1.0 m). In the present device, the distance from the polygon mirror to the sensor, i.e., $R \rightarrow M_4 \rightarrow S$, is 600 mm. For a depth of focus, Z_f , of 11.6 mm (the 10% defocussing case), the optical scanner allows a width of $\sim 24.0 \text{ cm}$ for which the laser spot size remains minimal (within a 10% defocussing) across the sensor. This geometry is shown in Fig.3.5. Although the present device does not satisfy the basic design criteria of a



a) Side view



* Not drawn to scale

b) Top view

Figure 3.4 Layout of the Optical Assembly

14 in. (or 36 cm) scan, the 3 sets of sensors used for testing the imaging system only have a width of 5 cm. Therefore, at this stage of development, the optical assembly is adequate for the data analysis experiments.

*Not drawn to scale

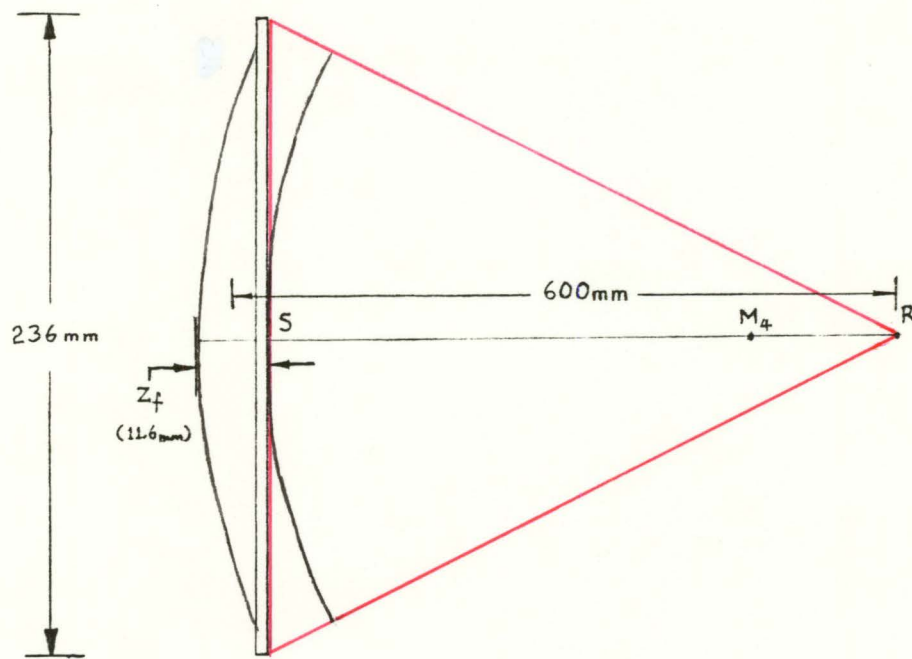


Figure 3.5 Geometry of a scan

CHAPTER 4

SENSOR ENERGETICS

At the present time, a complete physical model for how the sensor interacts with a combination of X-ray radiation and laser light is not fully understood. However, there are theoretical models that attempt to describe this kind of interaction. The following simple model is based on the work of Zermeno et al [7].

Consider the basic configuration of the sensor (Fig. 2.2) and the electronics of this system (Fig. 2.4) again. The sensor can be viewed as a parallel plate capacitor with two different kinds of dielectric materials, PbO and SiO, placed in between the plates (Fig. 4.1). The capacitance of the sensor is a combination of the capacitance of the PbO layer and the SiO layer, i.e.,

$$\frac{1}{C_{\text{sensor}}} = \frac{1}{C_{\text{PbO}}} + \frac{1}{C_{\text{SiO}}} \quad (4.1)$$

where C_{PbO} is the capacitance/unit area of the PbO layer, and C_{SiO} is the capacitance/unit area of the SiO layer.

Also, C_{PbO} and C_{SiO} are given by

$$C_{\text{PbO}} = \frac{K_{\text{PbO}} \epsilon_0}{d_{\text{PbO}}} \quad (4.2a)$$

and
$$C_{\text{SiO}} = \frac{K_{\text{SiO}} \epsilon_0}{d_{\text{SiO}}} \quad (4.2b)$$

where K_{PbO} , K_{SiO} are the dielectric constants of PbO and SiO, and d_{PbO} , d_{SiO} are the thickness of PbO and SiO layer, respectively. With a bias voltage, V , applied across the circuit (Fig. 2.4), the potential across the PbO layer is given as

$$V_{\text{PbO}} = \frac{2 V C_{\text{SiO}}}{C_{\text{SiO}} + C_{\text{PbO}}} \quad (4.3)$$

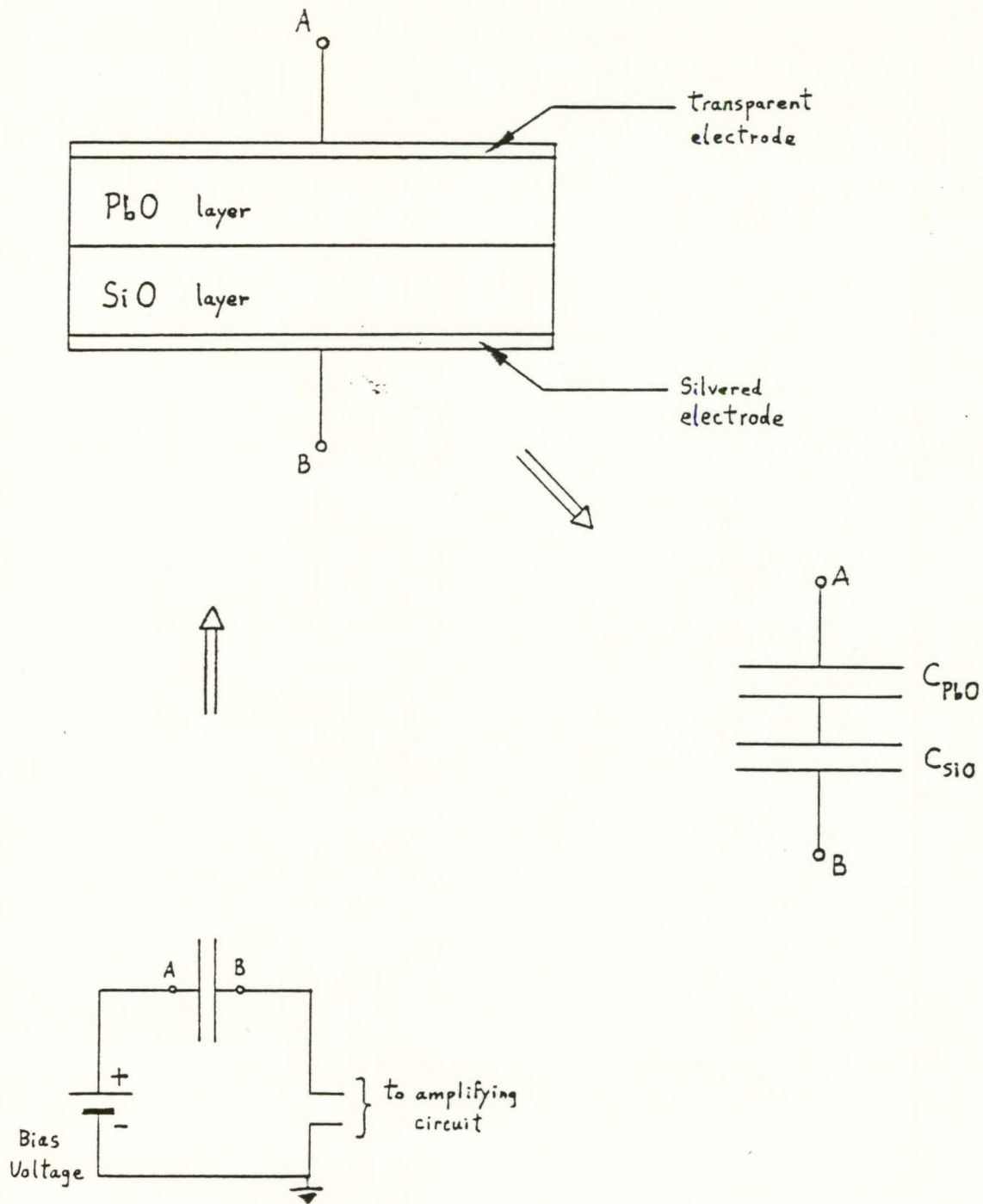


Figure 4.1 Structure of the Sensor as a Parallel Plate Capacitor

With incident laser light, the charge stored per unit area of the PbO layer, Q_{Laser} , will produce a photocurrent, expressed as the following equations,

$$Q_{\text{Laser}} = \frac{2 V C_{\text{SiO}_2}}{C_{\text{SiO}_2} + C_{\text{PbO}}} \quad (4.4a)$$

$$i_{\text{Laser}} = \frac{dQ_{\text{Laser}}}{dt} \quad (4.4b)$$

Eq.(4.4b) gives the value of the photocurrent, when no X-ray radiation has been absorbed by the sensor. However, if the sensor is exposed to radiation, then the value of the charge store is reduced in proportion to the radiation dose. i.e.,

$$Q_{\text{total}} = Q_{\text{laser}} - Q_{\text{X-ray}} \quad (4.5a)$$

Taking the time derivative of (4.5a) gives

$$i_{\text{meas}} = i_{\text{laser}} - i_{\text{X-ray}} \quad (4.5b)$$

The value of $Q_{\text{X-ray}}$ can be determined by defining the photogeneration efficiency

$$\eta = \frac{d\xi}{dn} E, \quad (4.6)$$

where ξ is the X-ray energy absorbed, n is the number of neutralized charge on the PbO layer, and E is the electric field across the PbO layer. Also, the number of neutralized charges, n , can be defined as

$$n = \frac{Q_x A}{e}, \quad (4.7)$$

where Q_x is the surfaced charge neutralized/unit area, A is the area of the PbO layer, and e is the elementary charge.

The X-ray energy absorbed by the PbO layer is defined as

$$\xi = fXA, \quad (4.8)$$

where f is the fraction of energy absorbed, and X is the intensity of X-ray.

Finally, the electric field across the PbO layer is

$$E = \frac{Q_{PbO}^*}{C_{PbO} d_{PbO}} \quad (4.9)$$

where Q_{PbO}^* is the instantaneous charge across the PbO layer.

Substituting Eqs.(4.9) (4,8) and (4.7) into Eq.(4.6) yields

$$\eta = \frac{feQ_{PbO}^*}{C_{PbO} d_{PbO}} \cdot \frac{dX}{dQ_x} \quad (4.10)$$

However Q_{PbO}^* can be expressed as

$$Q_{PbO}^* = \left[\frac{2VC_{PbO}C_{SiO}}{C_{PbO} + C_{SiO}} - Q_x \frac{C_{PbO}}{C_{PbO} + C_{SiO}} \right] \quad (4.11)$$

Combining Eqs.(4.10) and (4.11) yields

$$\begin{aligned} \eta &= \frac{fe}{C_{PbO} d_{PbO}} \left[\frac{2VC_{PbO} C_{SiO}}{C_{PbO} + C_{SiO}} - Q_x \frac{C_{PbO}}{C_{PbO} + C_{SiO}} \right] \frac{dX}{dQ_x} \\ \eta &= \left[\frac{2feVC_{SiO}}{(C_{SiO} + C_{PbO})d_{PbO}} - \frac{feQ_x}{(C_{SiO} + C_{PbO})d_{PbO}} \right] \frac{dX}{dQ_x} \\ \frac{dQ_x}{dX} &= \frac{2feVC_{SiO}}{(C_{SiO} + C_{PbO})d_{PbO}} - \frac{fe}{(C_{SiO} + C_{PbO})d_{PbO}} Q_x \\ \frac{dQ_x}{dX} + \frac{fe}{(C_{SiO} + C_{PbO})d_{PbO}} Q_x - \frac{2feVC_{SiO}}{(C_{SiO} + C_{PbO})d_{PbO}} &= 0 \quad (4.12) \end{aligned}$$

The solution to differential equation (4.12) is

$$Q_x = 2C_{SiO}V \left[1 - e^{-\frac{fe}{\eta(C_{SiO} + C_{PbO})d_{PbO}} X} \right] \quad (4.13)$$

The charge seen by the external circuit when Q_x is neutralized by X-rays is

$$\begin{aligned} Q_{X-ray} &= Q_x \left[\frac{C_{SiO}}{C_{SiO} + C_{PbO}} \right] \\ &= \frac{2VC_{SiO}^2}{C_{SiO} + C_{PbO}} \left[1 - e^{-\frac{fe}{\eta(C_{SiO} + C_{PbO})d_{PbO}} X} \right] \quad (4.14) \end{aligned}$$

Substituting Eq.(4.14) into Eq.(4.5) gives

$$Q_{total} = \frac{2VC_{SiO}^2}{C_{SiO} + C_{PbO}} - \frac{2VC_{SiO}^2}{C_{SiO} + C_{PbO}} \left[1 - e^{-\frac{fe}{\eta(C_{SiO} + C_{PbO})d_{PbO}} X} \right] \quad (4.15)$$

and upon illumination by laser light, Q_{total} , results in a photocurrent expressed as,

$$\begin{aligned} i_{meas} &= i_{laser} - i_{X-ray} \\ &= \frac{d}{dt} [Q_{laser} - Q_{X-ray}] \\ &= \frac{d}{dt} Q_{total} \quad (4.16) \end{aligned}$$

As mentioned in Chapter 2, this photocurrent, i_{meas} , is first amplified by a current-to-voltage converter amplifier, and then measured and stored by an oscilloscope (Fig. 2.5).

Most of the variables (or parameters) in Eq.(4.15) can be easily determined. The capacitance/unit area of PbO and SiO can be calculated using Eqs.(4.2a) and (4.2b). The dielectric constants of PbO and SiO are $K_{PbO} = 18$ and $K_{SiO} = 2$. The thickness of the two layers are given in Table II.1, Ch.2. Photogeneration Efficiency, η , is an intrinsic constant. The fraction of X-ray absorbed, f , by the sensor during an exposure, appears to be dependent on the energy of the dose (Fig. 4.2), results of the X-ray absorption tests of a sensor, indicate a linear relation between absorption and exposure.

At present, there are insufficient experimental data to fully demonstrate the validity of this theoretical model. However, the model can be used as a basis and a guide for improving the sensor performance. For example, Eq.(4.5b) suggests that the X-ray "image" information is given by

$$i_{X\text{-ray}} = i_{laser} - i_{meas}$$

Also, Eqs.(4.15) and (4.16) suggest that

$$0 < i_{meas} < i_{laser}$$

which means that the maximum $i_{X\text{-ray}}$ can have is i_{laser} . When there is no X-ray exposure, $i_{X\text{-ray}}$ is equal to 0. However, when there is strong X-ray exposure, $i_{X\text{-ray}}$ approaches i_{laser} . Therefore, the dynamic range of the "image" (i.e., gray scale \rightarrow black to white) can be improved by increasing i_{laser} .

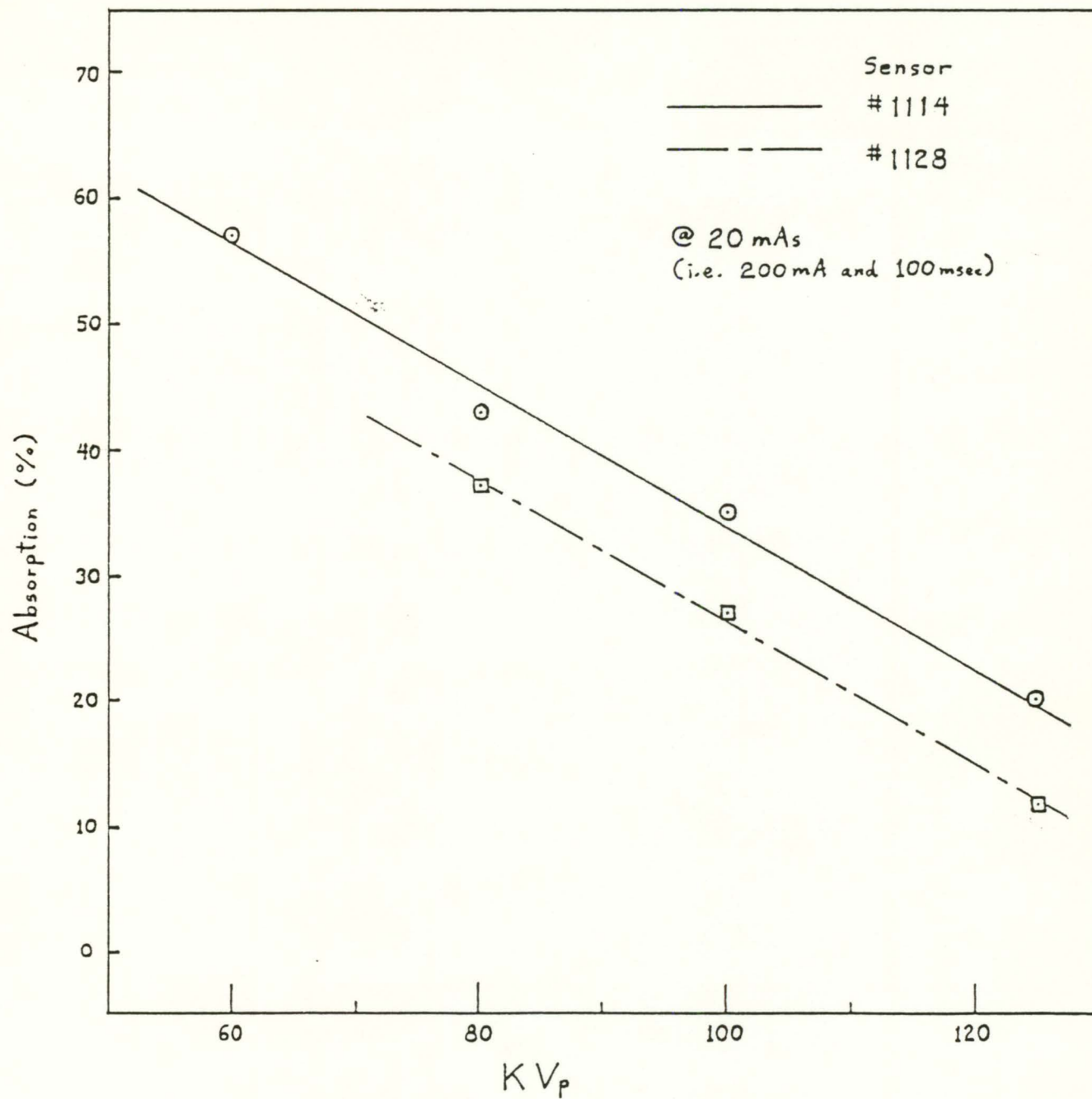


Figure 4.2 Percentage Absorption vs KVp of X-ray

CHAPTER 5

EXPERIMENTAL RESULTS

Initial testing of the new scanning device employed sensor #1126B with the test conditions given as: 30 volts dc applied to the sensor, and the scan speed set at 128, 256 or 512 lines/sec. Same experiments were repeated using sensors #1114B and #870A.

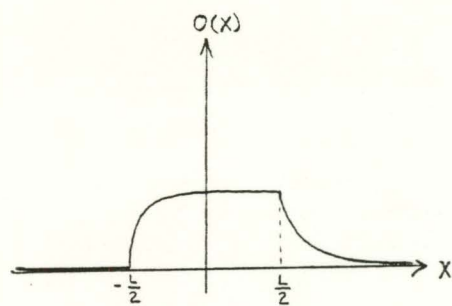
As mentioned in Chapter 2, the photocurrent from the sensor is first amplified by the current-to-voltage converter-amplifier. Next, the amplified waveform is collected and stored by a storage oscilloscope. Finally, the waveform is plotted using an X-Y recorder. The raw X-Y recorder data for each sensor (shown in Appendix I) uses the Y-axis for voltage and the X-axis for time measurement [3].

In Section 2.2, it was shown that every spatial position on the sensor is directly proportional to the time into the scan, which is given by

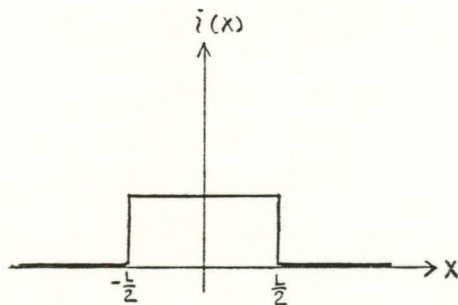
$$x = v \cdot t , \quad (5.1)$$

where x is the position on the sensor, v is the velocity of the laser flying spot on the surface of the sensor, and t is the time into the scan. Therefore, the time axis on the measured data, can be transformed easily into spatial position.

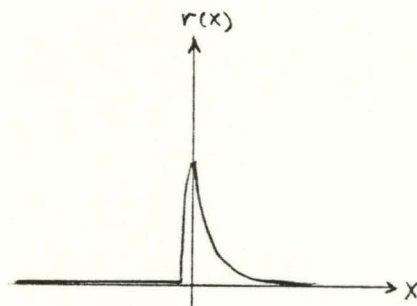
The data collected from a simple straight line scan (without any X-ray modulation) typically appears as a signal with a rising portion when the laser spot is on the sensor, and starts falling once the laser spot leaves the sensor (Fig. 5.1a). Ideally, the



a) Typical Optical waveform



b) Ideal Waveform



c) Response Function of the Sensor

Figure 5.1

signal should appear as a rectangular waveform (Fig. 5.1b), Unfortunately, no real system has such an ideal response. However, one can consider the measured signal as a convolution of the input signal (the rectangular wave) and the response function (Fig. 5.1c) of the sensor. Mathematically, this is expressed as,

$$\begin{aligned} o(x) &= i(x) \otimes r(x) \quad (\otimes - \text{convolution operator}) \\ &= \int_{-\infty}^{\infty} i(u) \cdot r(x-u) du, \end{aligned} \quad (5.2)$$

where $o(x)$ is the measured signal, $i(x)$ is the input function, and $r(x)$ is the response function.

The input function (in relative amplitude) and response function are represented by

$$i(x) = \begin{cases} 0 & x < -L/2 \\ 1.0 & -L/2 < x < L/2 \\ 0 & x > L/2 \end{cases}, \quad (5.3)$$

$$\text{and } r(x) = \begin{cases} 0 & x < -h \\ r_1 (1 - e^{-\mu_c(x+h)}) & -h < x < 0 \\ A e^{-\mu_d x} & x > 0 \end{cases} \quad (5.4)$$

respectively, where L is the width of the sensor (5 cm in this case), μ_c and μ_d are the rise and fall (or charge and discharge) constants of the sensor, respectively. The parameters

$$h = \frac{1}{\mu_c}$$

$$\text{and } A = r_1 (1 - e^{-\mu_c h})$$

are defined such that $r(x)$ is continuous at x equal to 0. Also, the parameter r_1 is defined as

$$r_1 = \frac{e}{\left[\frac{1}{\mu_c} + \frac{e-1}{\mu_d} \right]}$$

for normalization purpose. This gives

$$\int_{-\infty}^{\infty} r(x) \cdot dx = 1.0 . \quad (5.5)$$

The rise and fall constants of each sensor at different scan speed are estimated from the experimental waveforms (Table V.1). In Chapter 6, the experimental data are analysed and compared, and conclusions are stated.

Table V.1 Amplitudes, rise and fall constants of each sensor at scanspeeds 128, 256 and 512 lines/sec

Scan-speed (lps)	sensor #870A			sensor #1114B			sensor #1126B		
	μ_c	μ_d	V_{max}	μ_c	μ_d	V_{max}	μ_c	μ_d	V_{max}
128	0.1359	0.1280	0.550	0.7349	0.3812	0.950	1.5238	1.0166	0.188
256	0.2089	0.0750	0.325	0.3813	0.2310	0.650	0.8860	0.6100	0.170
512	0.2887	0.0673	0.200	0.2298	0.1277	0.400	0.5573	0.3812	0.138

Note : μ_c and μ_d are the rise and fall constants (cm⁻¹)
 V_{max} is the amplitude (Volts)

CHAPTER 6

DATA ANALYSIS

From the waveforms obtained during the experiments, the rise and fall constants of each sensor at different scan speeds are estimated (Chapter 5, Table V.1). These results are used to calculate the response function of the sensors. In this chapter, the MTF (Modulation Transfer Function) of the sensors are derived from their response functions. Then these MTFs are used for analysis and comparison.

6.1 MTF Definition

As discussed in Chapter 5, the output waveform obtained from the sensor (Fig. 6.1), resulting from a scan, is considered to be the convolution of an input function (Fig. 6.2) and a response function (Fig. 6.3), expressed mathematically in Eq.(5.2) as

$$o(x) = i(x) \otimes r(x)$$

First, consider taking the Fourier transform of each function in Eq.(5.2). Instead of integration in the space-domain, the procedure becomes multiplication in the spatial-frequency-domain

[8,9]; i.e., if $O(s) = \mathcal{F}[o(x)]$,

$$I(s) = \mathcal{F}[i(x)] ,$$

and $R(s) = \mathcal{F}[r(x)]$;

where $\mathcal{F}[f(x)] = F(s) = \int_{-\infty}^{\infty} f(x) \cdot e^{i2\pi xs} dx$

Eq.(5.2) can be put in the form of:

$$O(s) = I(s) \cdot R(s) . \quad (6.1)$$

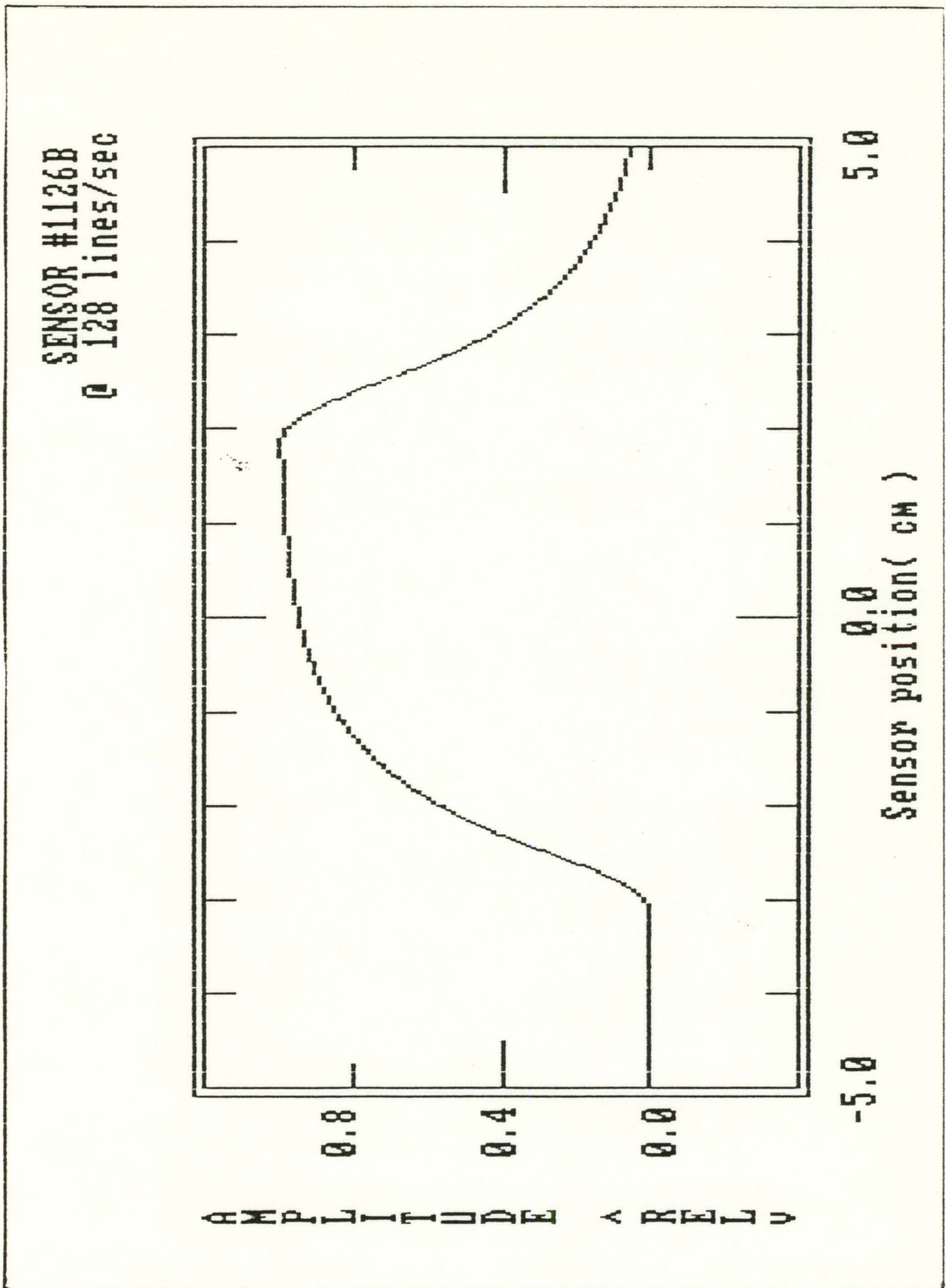


Figure 6.1 Optical Waveform of Sensor #1126B

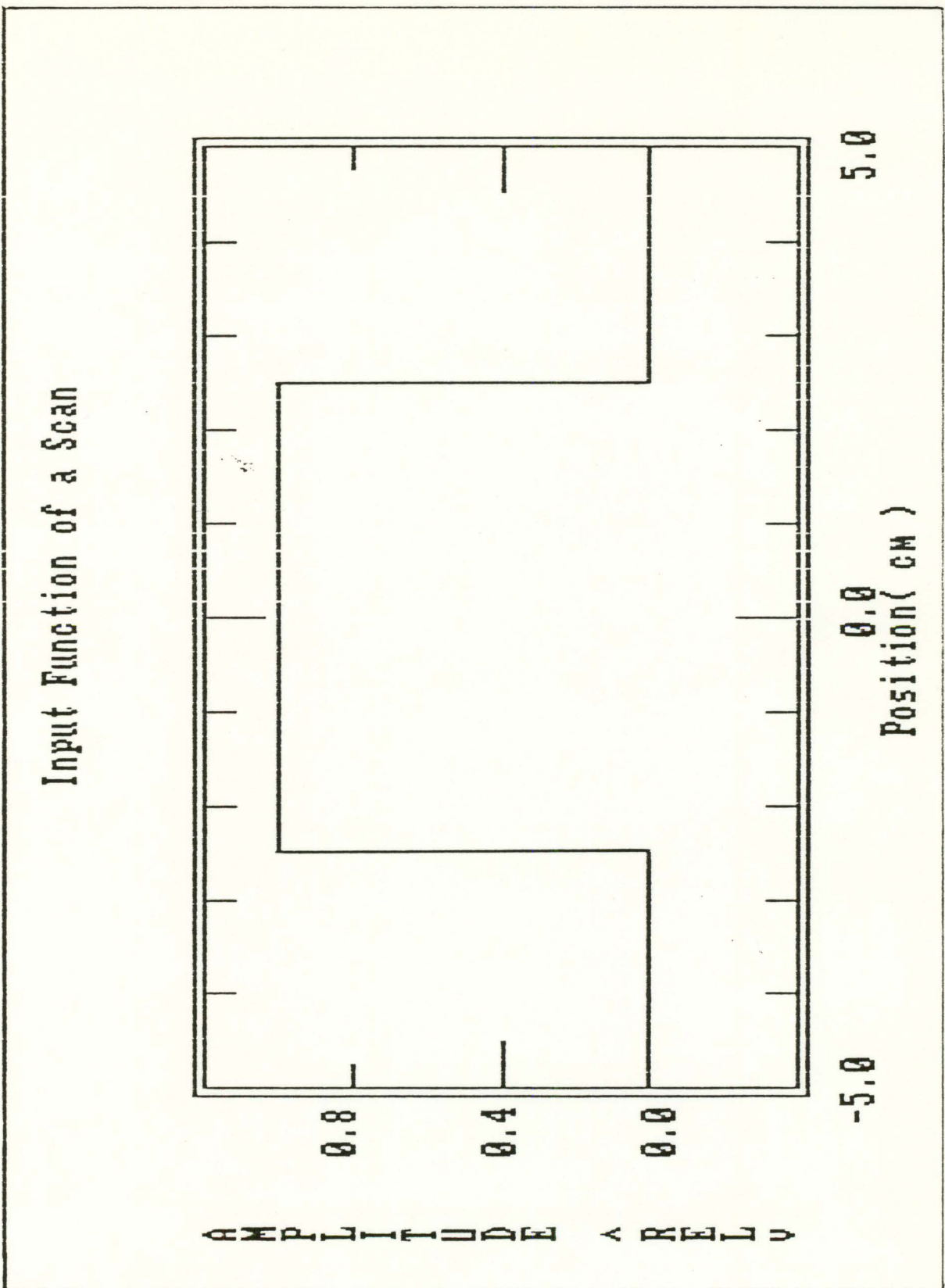


Figure 6.2 Input Function

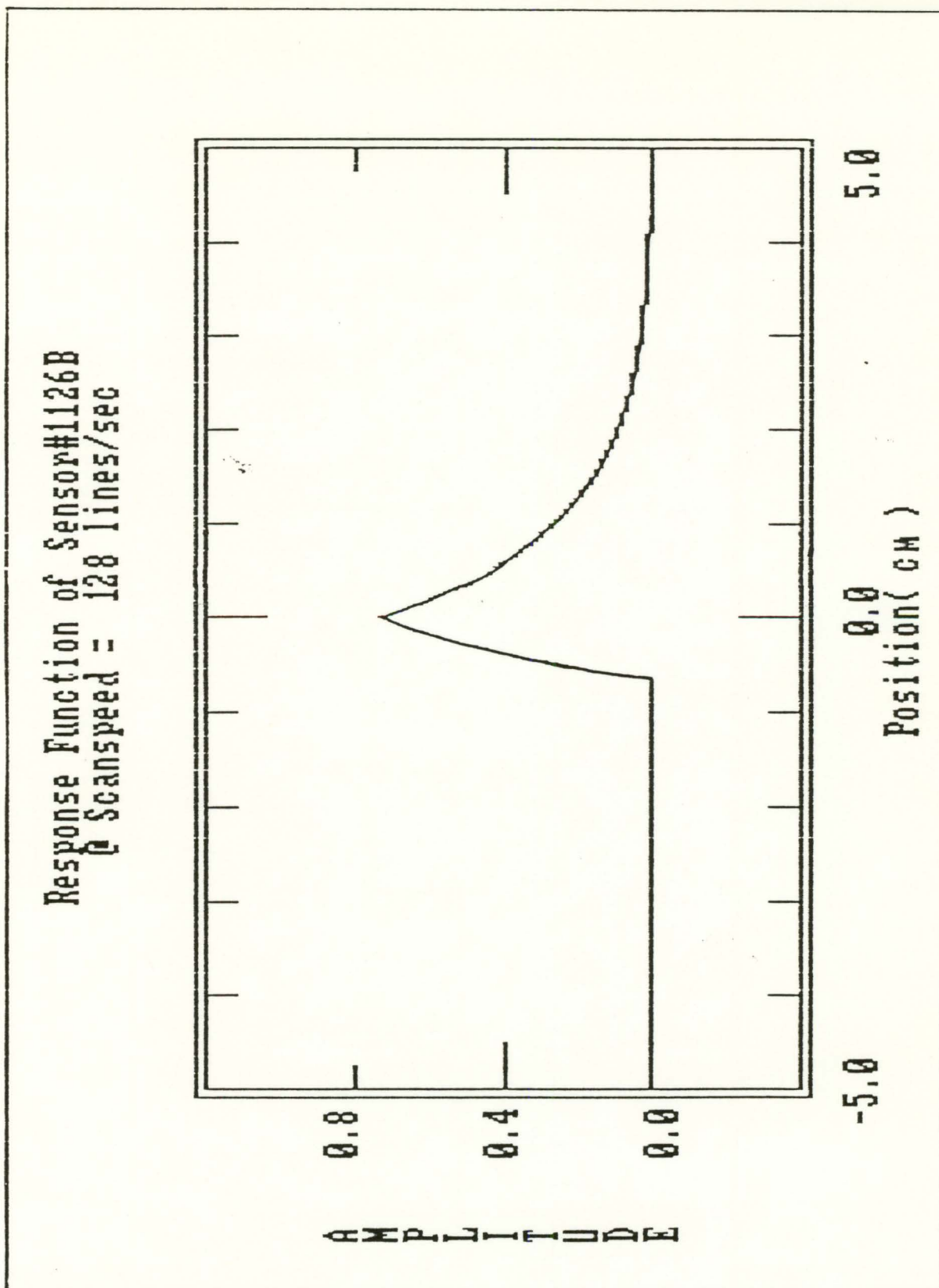


Figure 6.3 Response Function of Sensor #1126B

The MTF is defined as the Modulus of the Fourier Transform of the response function of the sensor [10], i.e.,

$$\begin{aligned} \text{MTF}(s) &= | \mathcal{F}[r(x)] | \\ &= | R(s) | \\ &= [R(s) \cdot R^*(s)]^{1/2}, \end{aligned} \quad (6.2)$$

where $R^*(s)$ is the complex conjugate of $R(s)$.

The MTF, which is a function of spatial frequency, is used as a measurement of the image quality of a particular system. To understand this, one should take several steps backward to Eq.(5.2). In an ideal imaging system, the response function is a delta-function (i.e., $r(x) = \delta(x)$) defined by [9],

$$\delta(x) = 0 \quad \text{for } x \neq 0, \quad (6.3a)$$

$$\int_{-\infty}^{\infty} \delta(x) dx = 1.0. \quad (6.3b)$$

Furthermore, the delta-function has the property that

$$\int_{-\infty}^{\infty} f(x) \delta(x-x_0) dx = f(x_0). \quad (6.3c)$$

Therefore, if the response function is a δ -function, then the output signal is equal to the input signal; i.e.,

$$\begin{aligned} o(x) &= i(x) \otimes r(x) \\ &= i(x) \otimes \delta(x) \\ &= \int_{-\infty}^{\infty} i(u) \delta(x-u) du \\ &= i(x). \end{aligned} \quad (6.4)$$

In this case, the MTF of the system would be,

$$\begin{aligned} \text{MTF}(s) &= | \mathcal{F}[r(x)] | \\ &= | \mathcal{F}[\delta(x)] | \\ &= 1.0 \end{aligned} \quad (6.5)$$

for all spatial frequencies, i.e., $0 < s < \infty$.

Therefore, in an ideal imaging system, the MTF is equal to 1.0 for all s values. However, in practice the response function is

not a δ -function, but it is a function with finite width, and finite duration of rising and falling portions. Thus, the MTF will always be less than or equal to 1.0 for any value of s .

6.2 MTF Calculation

The response function, $r(x)$, of the sensor, defined in Chapter 5, Eq.(5.4) is expressed as

$$r(x) = \begin{cases} 0 & x < -h \\ r_1 (1 - e^{-\mu_c(x+h)}) & -h < x < 0 \\ A e^{-\mu_d x} & x > 0 \end{cases}$$

where μ_c and μ_d are the rise and fall constants, respectively,

$$h = \frac{1}{\mu_c}$$

and

$$A = r_1 \left(1 - \frac{1}{e}\right)$$

such that $r(x)$ is continuous at x equal to 0. Also, from Eq.(5.5), the normalization factor is given as

$$r_1 = \frac{e}{\left[\frac{1}{\mu_c} + \frac{e-1}{\mu_d}\right]}$$

From Eq.(6.2), the MTF of the sensor is defined as

$$\text{MTF}(s) = [R(s) \cdot R^*(s)]^{1/2},$$

where $R(s)$ is the Fourier transform of $r(x)$, i.e.

$$R(s) = \int_{-\infty}^{\infty} r(x) e^{i2\pi x s} dx \quad (6.6)$$

For $r(x)$ defined as Eq.(4.4), $R(s)$ would be equal to

$$R(s) = r_1 \left[h e^{i\pi h s} \text{sinc}(hs) - \frac{(e^{-1/e})}{\mu_c + i2\pi s} + \frac{(1-1/e)}{\mu_d + i2\pi s} \right], \quad (6.7)$$

where s is the spatial frequency (i.e. cycles/cm).

6.3 Analysis

The MTF is a measurement of image quality. By defining a minimum MTF value acceptable to an imaging system (0.03 for commercial TV set), then there would be a corresponding maximum s value on the MTF versus s plot. This maximum s value is commonly defined as the limiting resolution of the particular imaging system [10].

The minimum acceptable MTF value is 0.001 for the imaging system studied in this project [11]. From the plots of MTF versus s for each sensor at different scan speeds (Fig. 6.4 to 6.12), the limiting resolution of each sensor is determined. As an example, take sensor #1126B at scan speed of 128 lines/sec (Fig. 6.4). For all MTF values greater than or equal to 0.001, the corresponding maximum possible s value is ~ 8.5 cycles/cm. Thus, the limiting resolution of sensor #1126B at a scan speed of 128 lines/sec is 8.5 cycles/cm. This means that the sensor can resolve a maximum of 8.5 spots in a region of 1.0 cm wide. Alternatively, the minimum resolvable spot size is given as the reciprocal of the limiting resolution, i.e.,

$$\begin{aligned} \frac{1}{8.5 \text{ cm}^{-1}} &= 0.12 \text{ cm} \\ &= 1.2 \text{ mm} \end{aligned}$$

for this particular case. Similarly, the limiting resolutions of the other cases were determined, and the results are tabulated in Table VI.1. These results show that sensor #1126B has the highest resolution of all three, followed by sensor #1114B and sensor #870A. In addition, the results show that scanning at a slow speed improves the image resolution, except for the case of sensor #870A, which seems to be independent of the scan speed.

Figure 6.4 MTF vs s for Sensor #1126B at Scanspeed 128 lines/sec

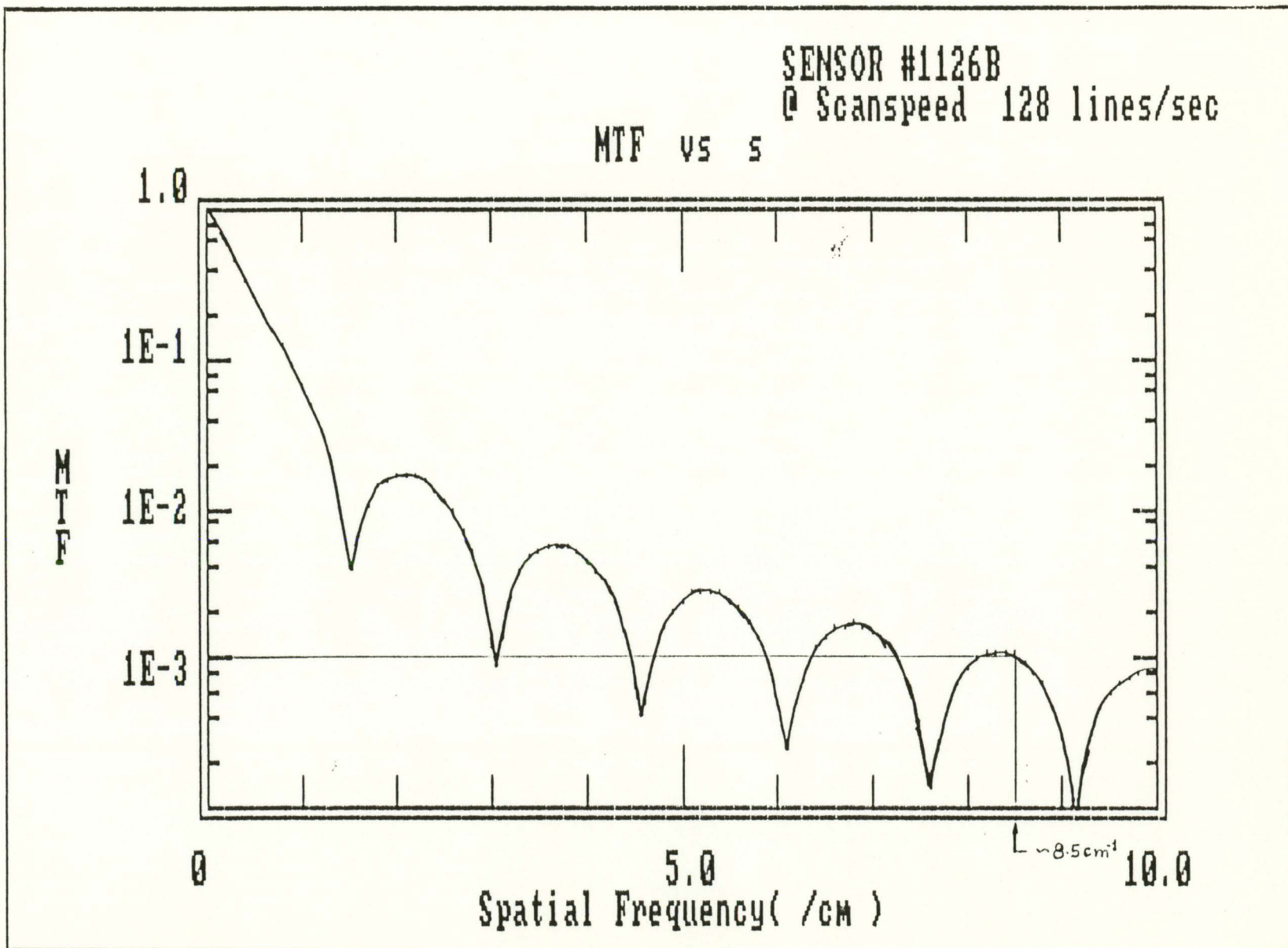


Figure 6.5 MTF vs s for Sensor #1126B at Scanspeed 256 lines/sec

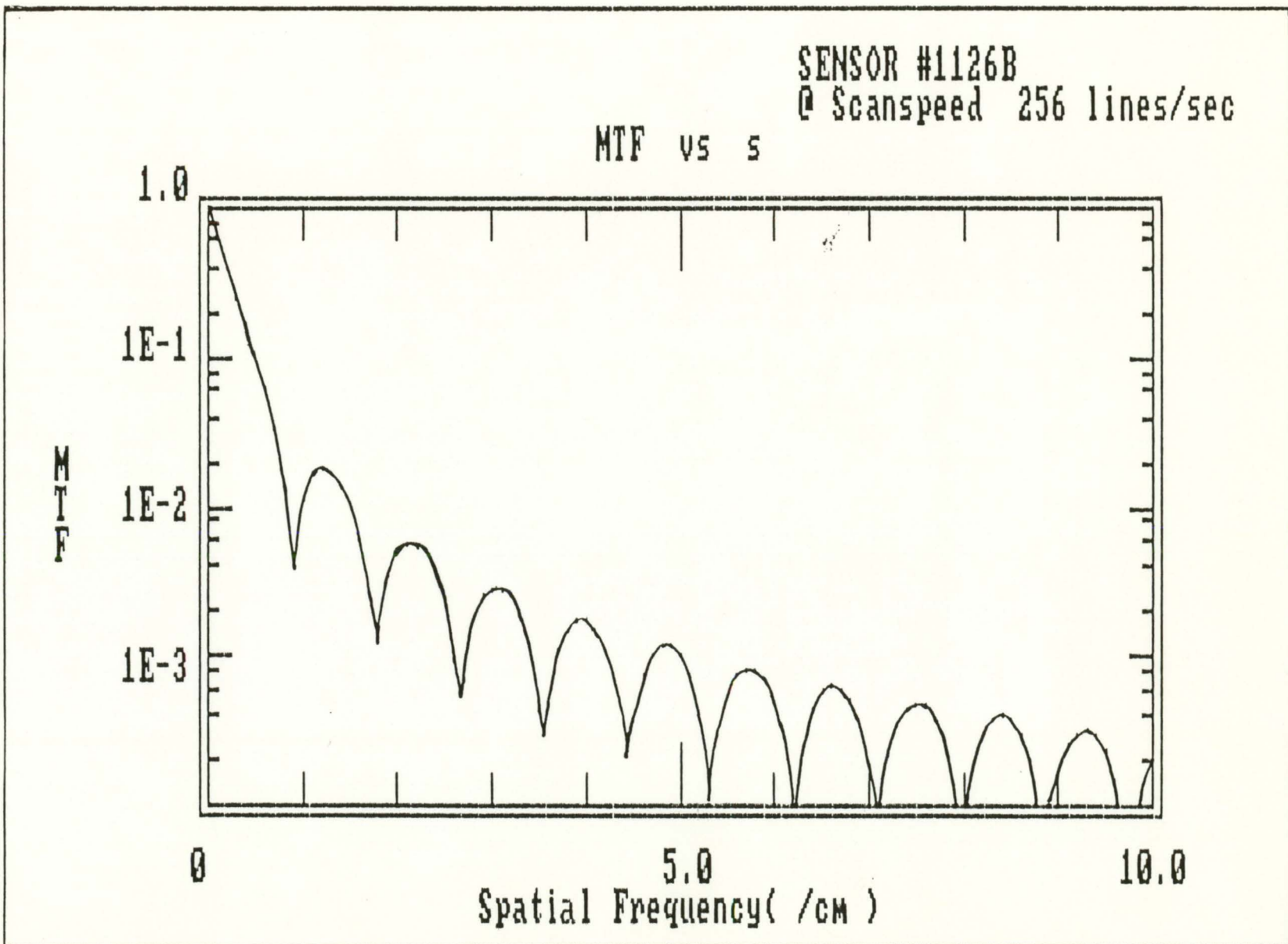


Figure 6.6 MTF vs s for Sensor #1126B at Scanspeed 512 lines/sec

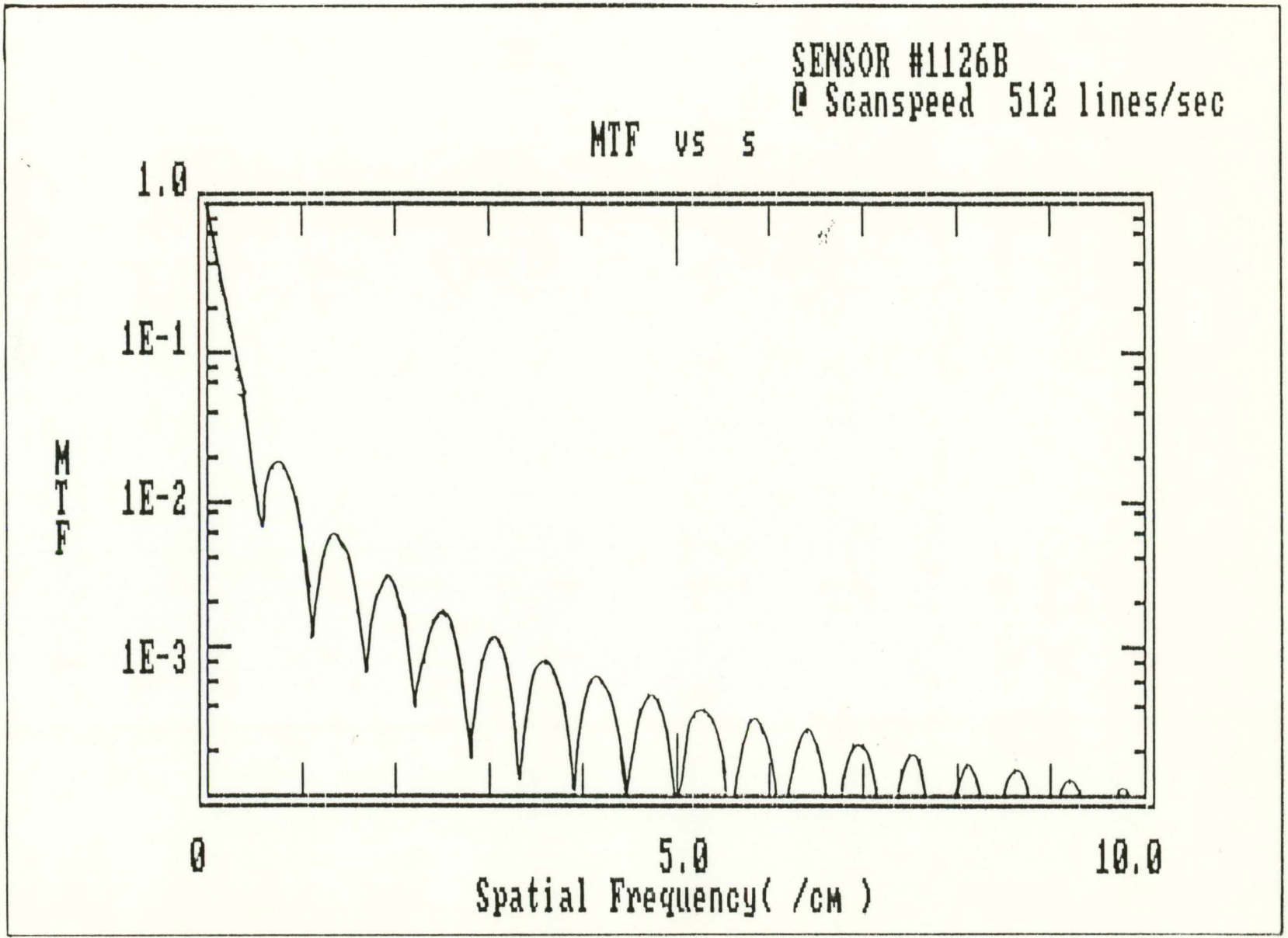


Figure 6.7 MTF vs s for Sensor #1114B at Scanspeed 128 lines/sec

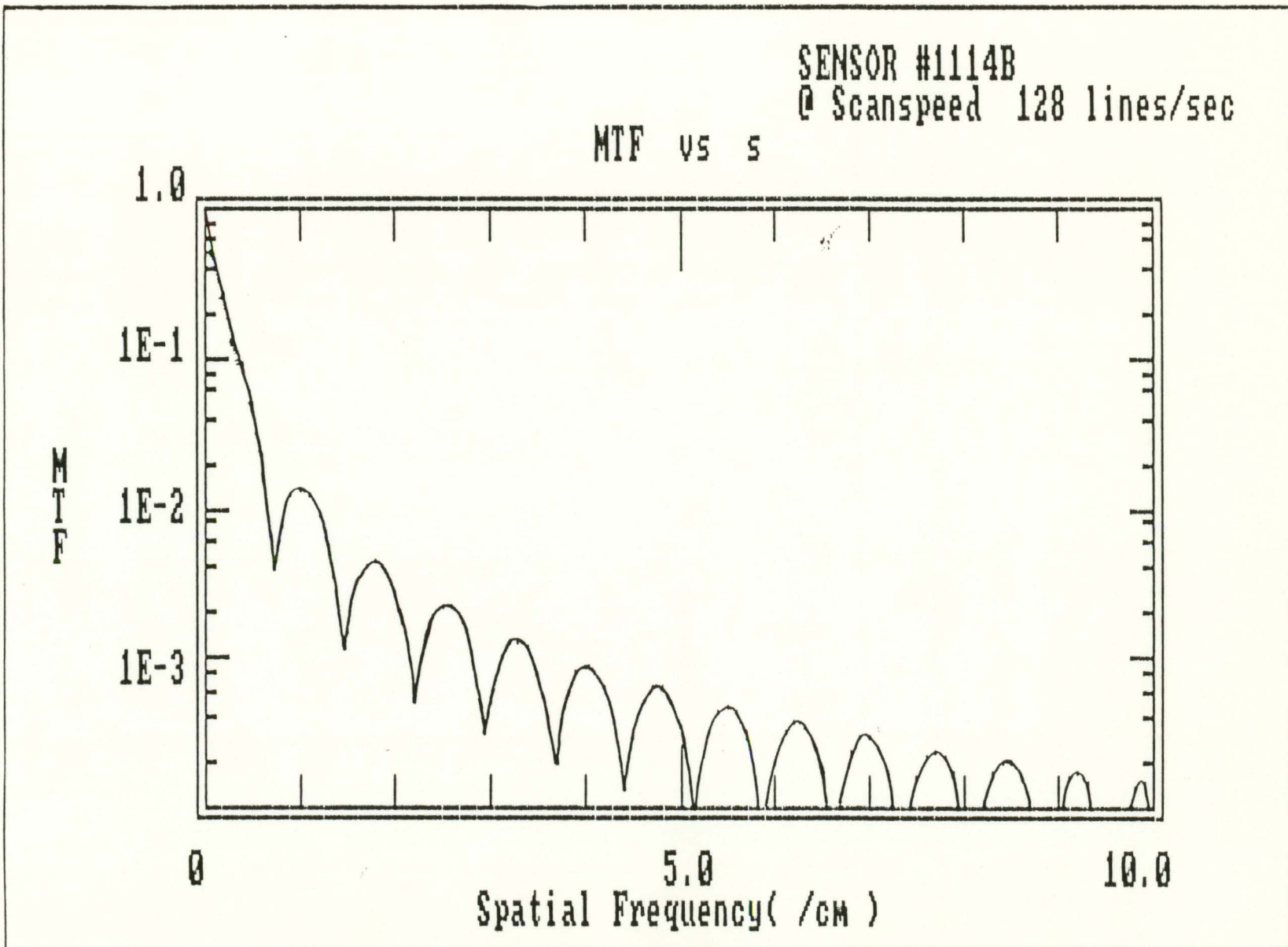


Figure 6.8 MTF vs s for Sensor #1114B at Scanspeed 256 lines/sec

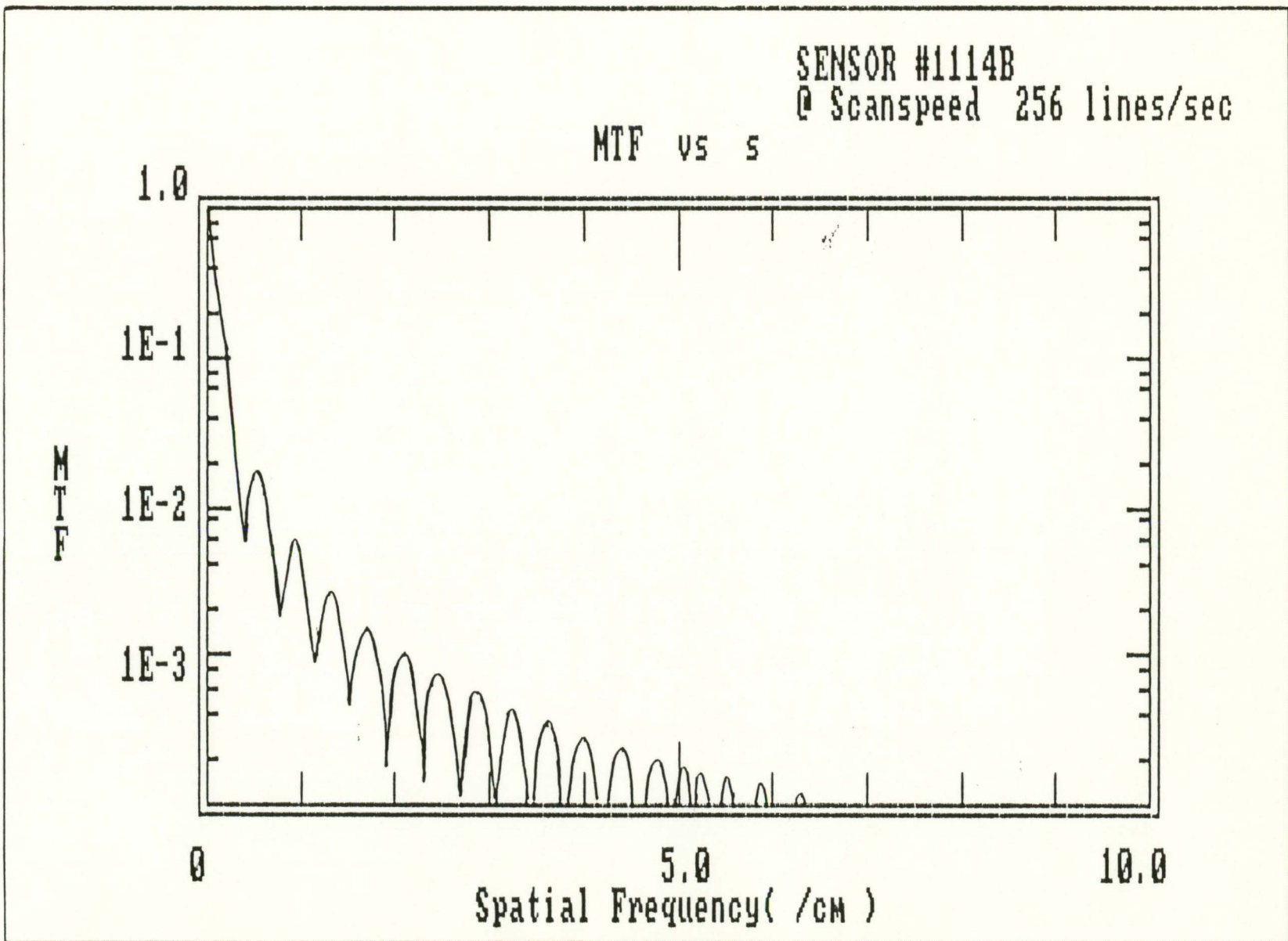


Figure 6.9 MTF vs s for Sensor #1114B at Scanspeed 512 lines/sec

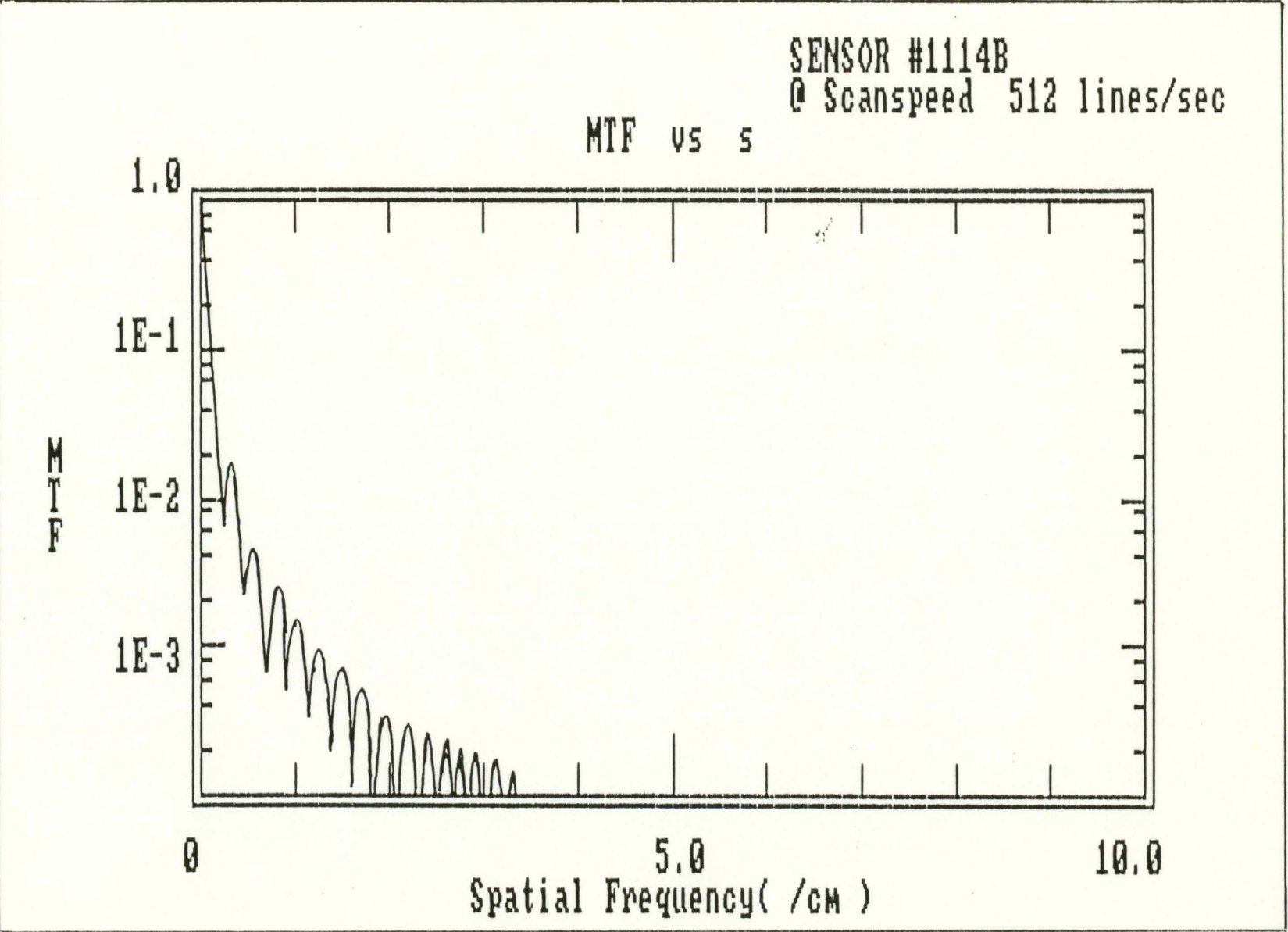


Figure 6.10 MTF vs s for Sensor #870A at Scanspeed 128 lines/sec

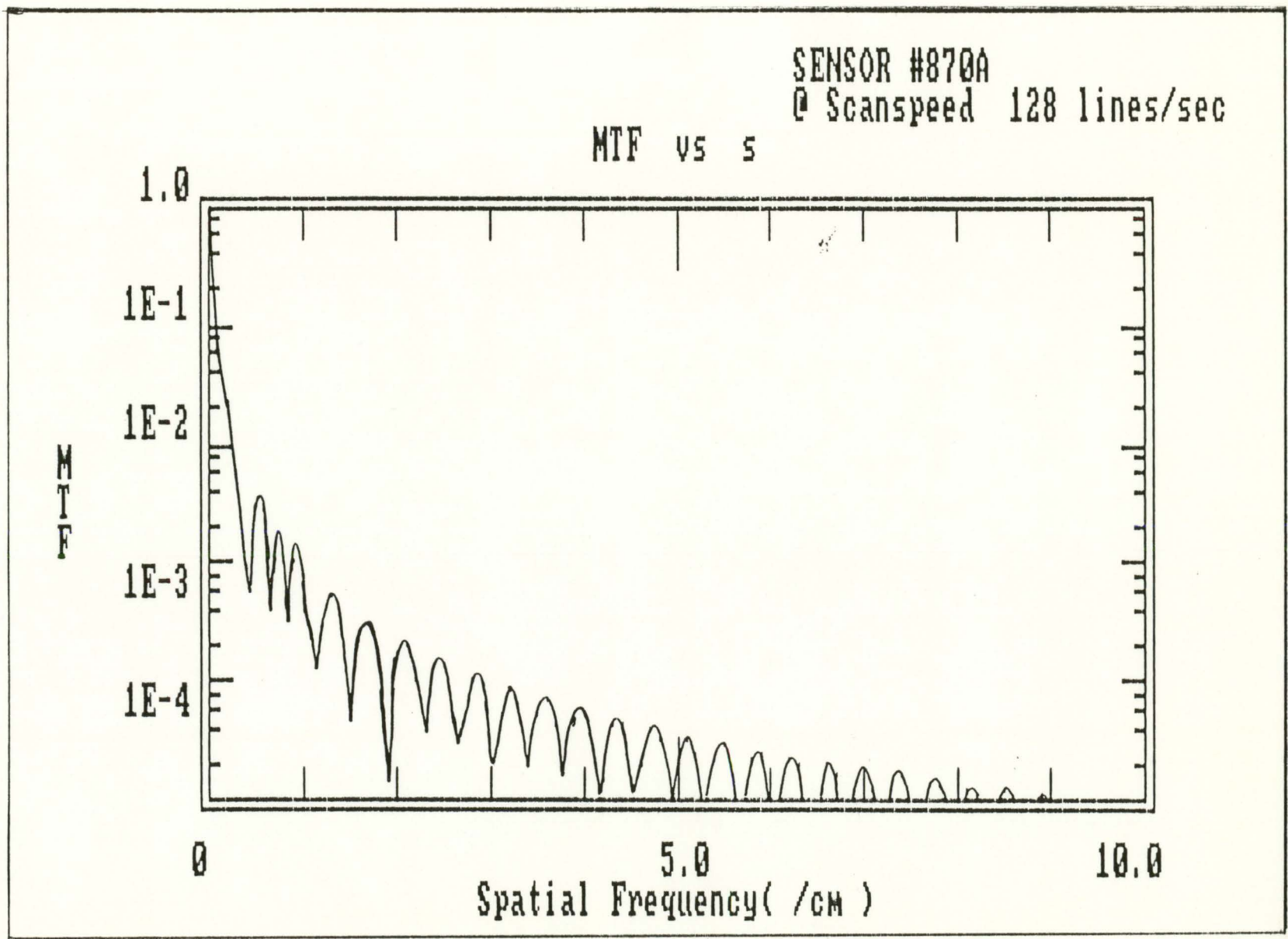
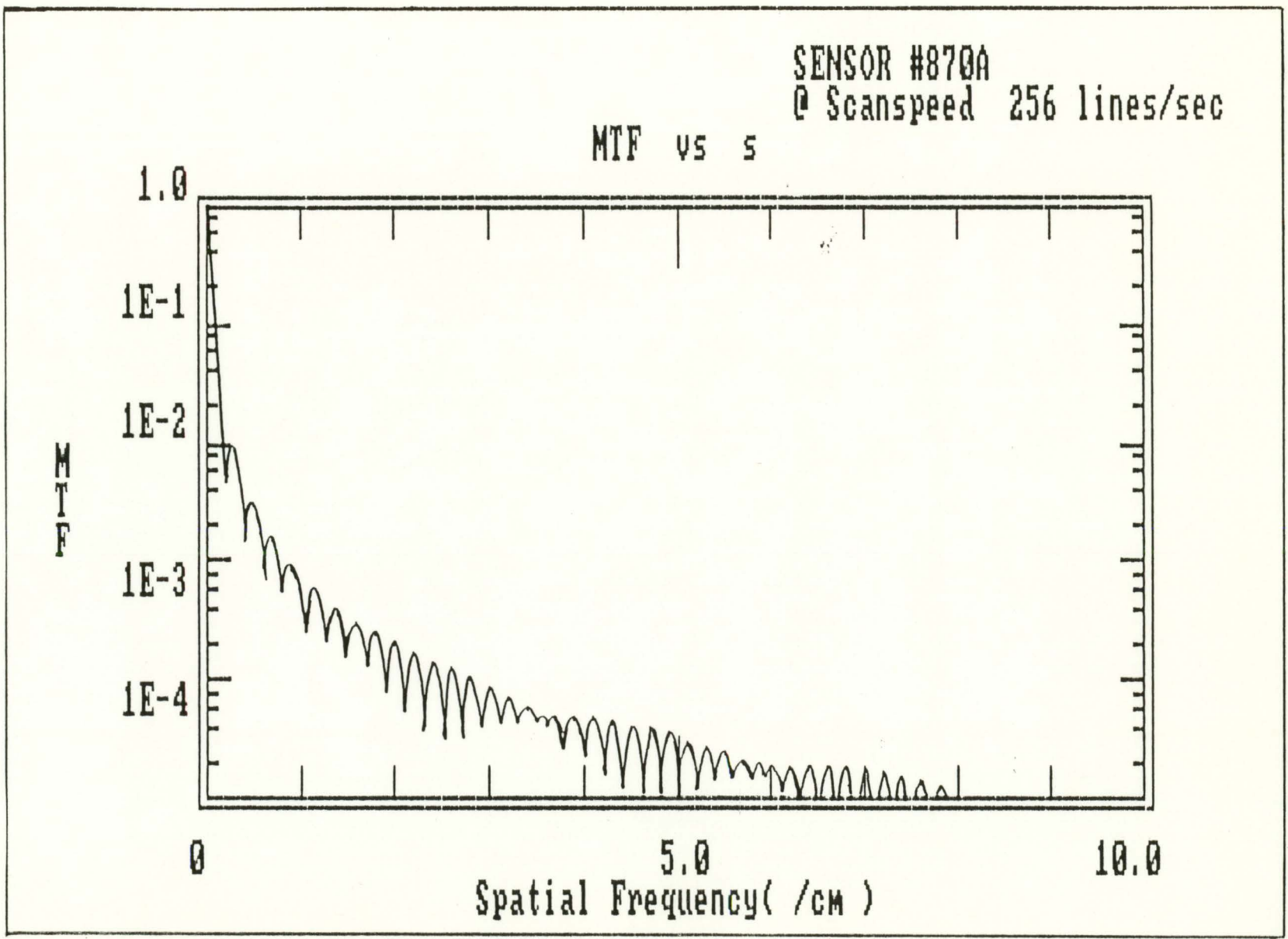


Figure 6.11 MTF vs for Sensor #870A at Scanspeed 256 lines/sec



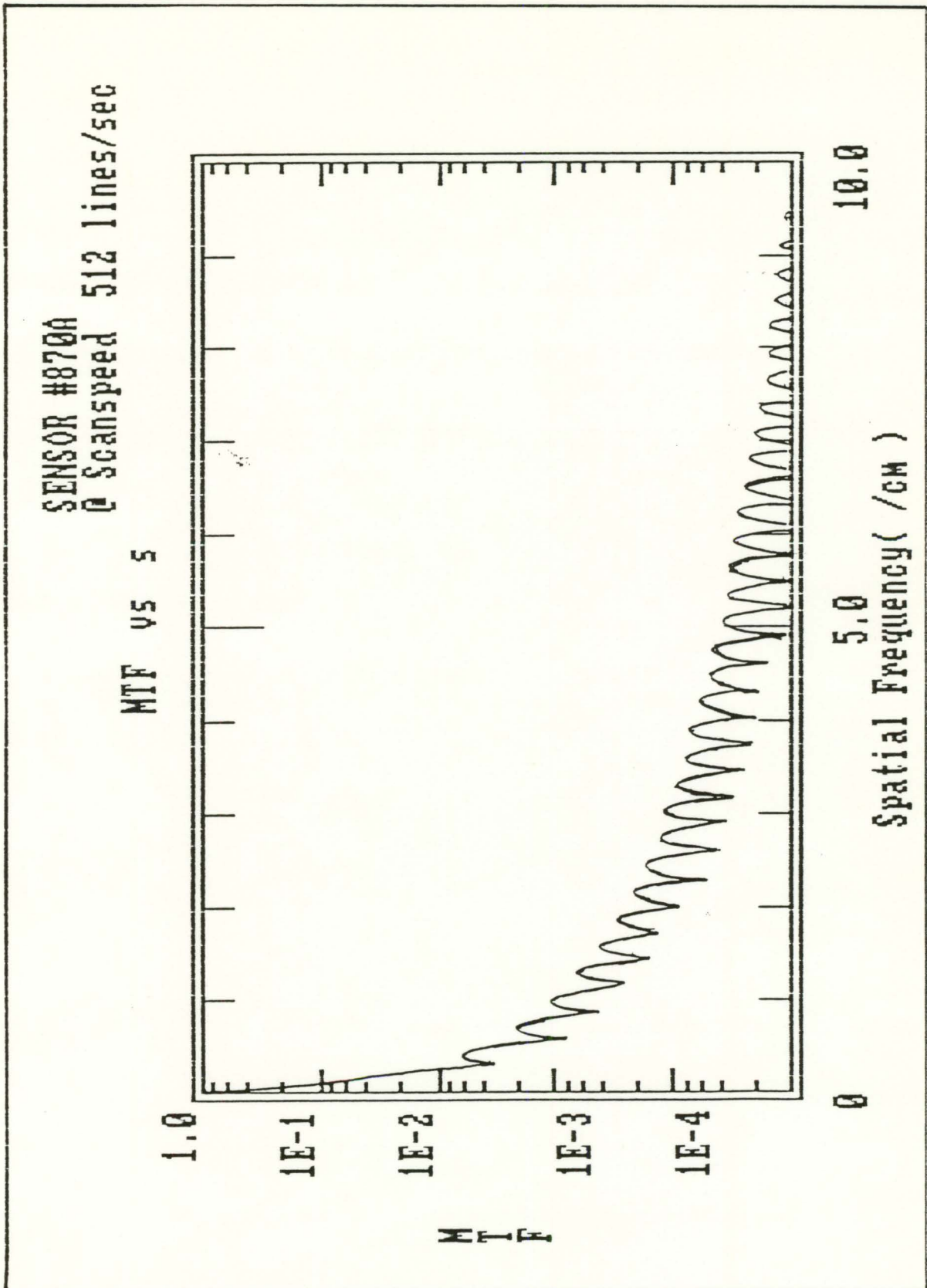


Figure 6.12 MTF vs s for Sensor #870A at
at Scanspeed 512 lines/sec

CHAPTER 7

CONCLUSIONS AND RECOMMENDATIONS

By the end of the summer of 1986, the optical assembly was built, and several experiments were carried out using this assembly to test the optical resolution of the sensors. In addition, X-ray absorption tests on the sensors were completed, and a theoretical model describing the sensor response to X-ray and laser light is also presented.

From the optical tests and the data analysis on the three different sensors presented in Chapter 6, it was shown that sensor #1126B has the highest resolution, followed by sensor #1114B and sensor #870A. Also, the results presented in Chapter 5 indicate that sensor #1114B has the strongest signal amplitude, followed by sensor #870A and sensor #1126B (note that sensor #870A is from the prototype of the feasibility study carried out in 1984). Due to the limitation of time, no X-ray exposure were done using this imaging system. However, from the feasibility study carried out 2 years ago, actual X-ray images were developed [2]. Therefore, once it is possible to carry out the X-ray exposure test with this imaging system, then comparison can be made with the theoretical model presented in Chapter 4.

Once again, the major achievements for this project over this summer can be summerized as the following:

- i) the optical signal gain of the new sensors are higher than the old sensor, and the signal-to-noise ratio is also improved [3];

- ii) the new sensors have faster response to an optical scan, thus higher optical resolution;
- iii) a new optical scanner assembly was built, with much higher mechanical stability than the old model, and with the laser spot size focussed down to $\sim 100 \mu\text{m}$, and an effective scan width of 24 cm (i.e., where the laser spot size remains minimal), and finally,
- iv) the optical resolution achieved for this system is ~ 10 cycles/cm, i.e. minimum resolvable object is ~ 1 mm in diameter.

Even with the successes to date, there are still several areas that need to be investigated. The first obvious area is to start the X-ray exposure measurement on test targets using this system, and then to compare the results with the theoretical model presented in Chapter 4. The structure of the sensor should also be changed as well. At present, the glass substrate side faces the optical assembly and the silvered electrode side faces the X-ray tube. When the laser spot hits the sensor, it passes through the glass medium first, which causes dispersion of the laser beam. This dispersion could severely affect the resolution of the system. Therefore, it would be advisable to modify the sandwich structure of the sensor (Fig. 2.2); i.e., set layer 2 to be the silvered electrode and layer 5 to be the transparent electrode, and have the glass substrate side face the X-ray tube and the transparent electrode side face the optical assembly. Thus, results in much reduced dispersion. The resolution would be improved if the

response of X-ray sensor is faster (i.e., faster rise and fall time). This would involve the detailed study of the solid-state physics of the sensor's material. Another recommendation is the use of a holographic disk (produced by PULSON INDUSTRIES, INC and HOLOTEK) as the scanner, rather than the polygon mirror. With the polygon mirror, the performance is susceptible to the mechanical vibration of its dc drive motor. The holographic disk is almost immune to wobble in the motor [12]. Finally, a fast computerized data acquisition system is required, in order to achieve any significant improvement on the present system.

REFERENCES

1. Thin Film Mammography - Project Proposal for I.R.A.P.; N.Ramanathan; Picker International Canada(internal report); 1985.
2. Final Project Report on Large Format Sensor Feasibility - The Laser Scanned X-ray Imaging System; N.Ramanathan; Picker International Canada(internal report); 1985.
3. Report on Design of Front End Wide Band Amplifier for Large Area Sensor for X-ray Imaging System; Q.Nguyen, T.Khosla; Picker International Canada(internal report); 1986.
4. Laser Electronics; J.T.Verdeyen; Prentice-Hall; 1981.
5. Optical Electronics; A.Yariv; Holt-Rinehart and Winston; 1985.
6. Optics Guide 3; Melles Griot; 1985.
7. Laser Readout of Electrostatic Images; A.Zermeno et al; SPIE Vol.173, Application of Optical Instrumentation in Medicine VII; 1979.
8. Fourier Transform and its Applications, 2nd Edition; R.N.Bracewell; McGraw Hill; 1978.
9. Mathematical Methodes for Physicists, 2nd Edition; G.Arffen; 1980.
10. Phase Effect in Diagnostitc Radiological Images; J.E.Gray, M.Trefler; Medical Physics, Vol.3, No.4, Jul/Aug 1976.
11. Private Communication; N.Ramanathan; 1986.
12. Hologon Laser Scanner for Non-impact Printing; C.J.Kramer; SPIE Proceeding, Vol.390, 1983.

APPENDIX I :-

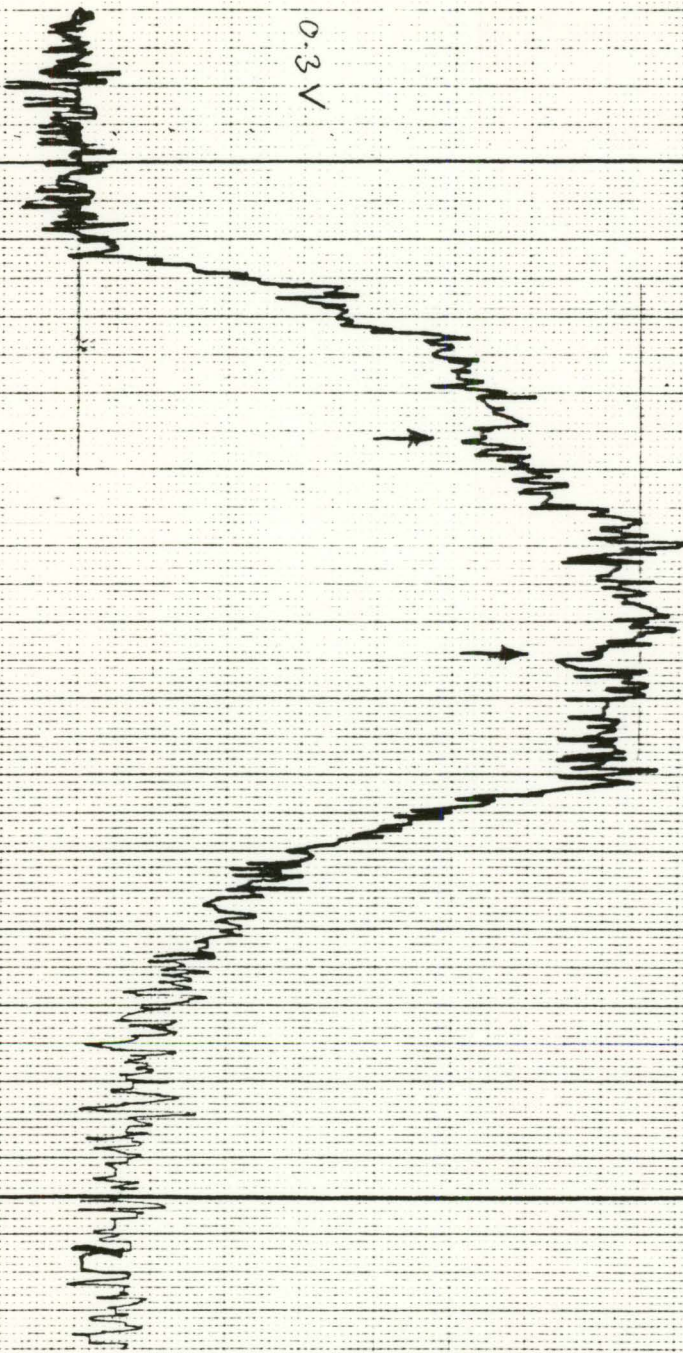
RAW DATA

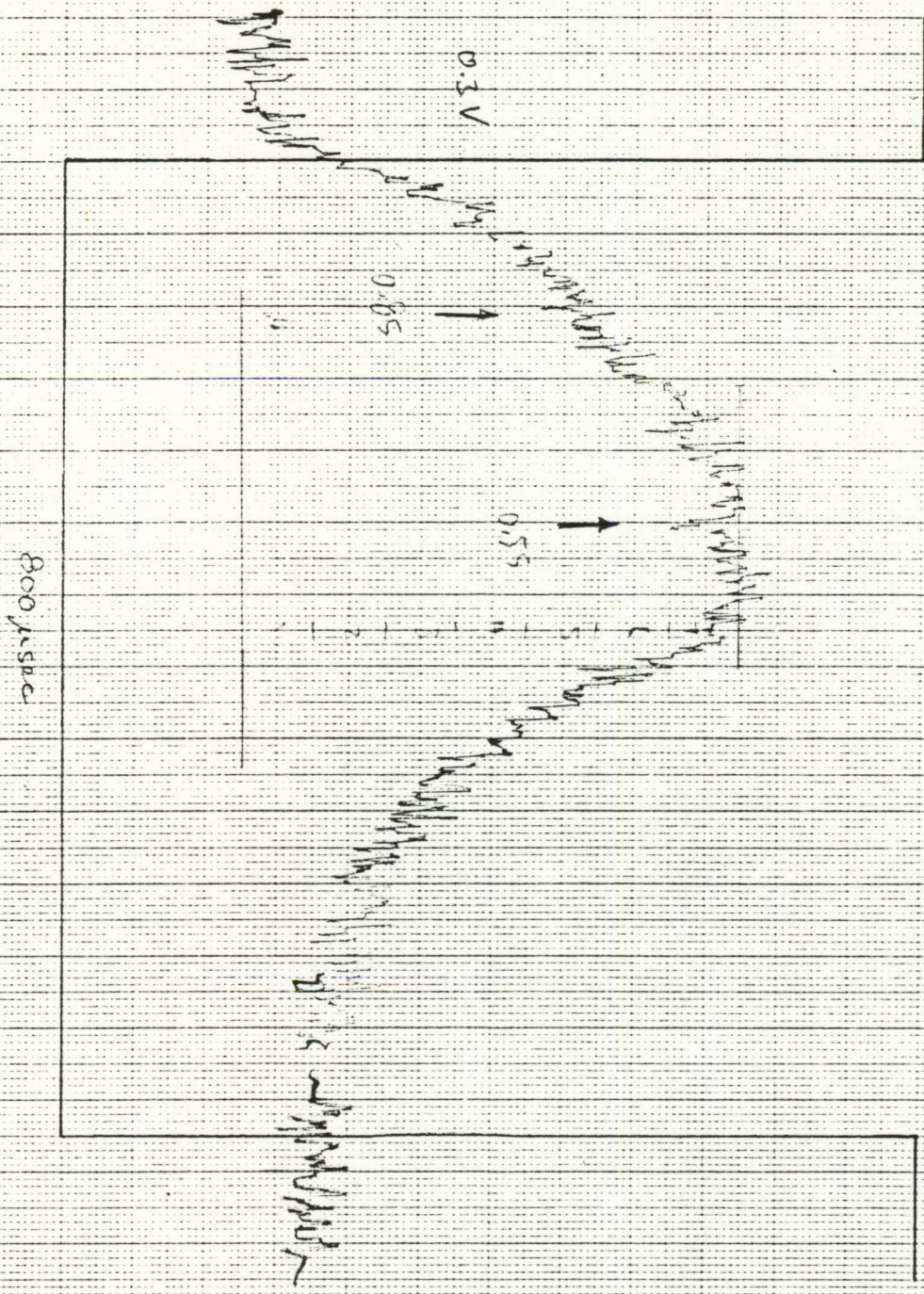
@ 128 lines/sec

1126 B

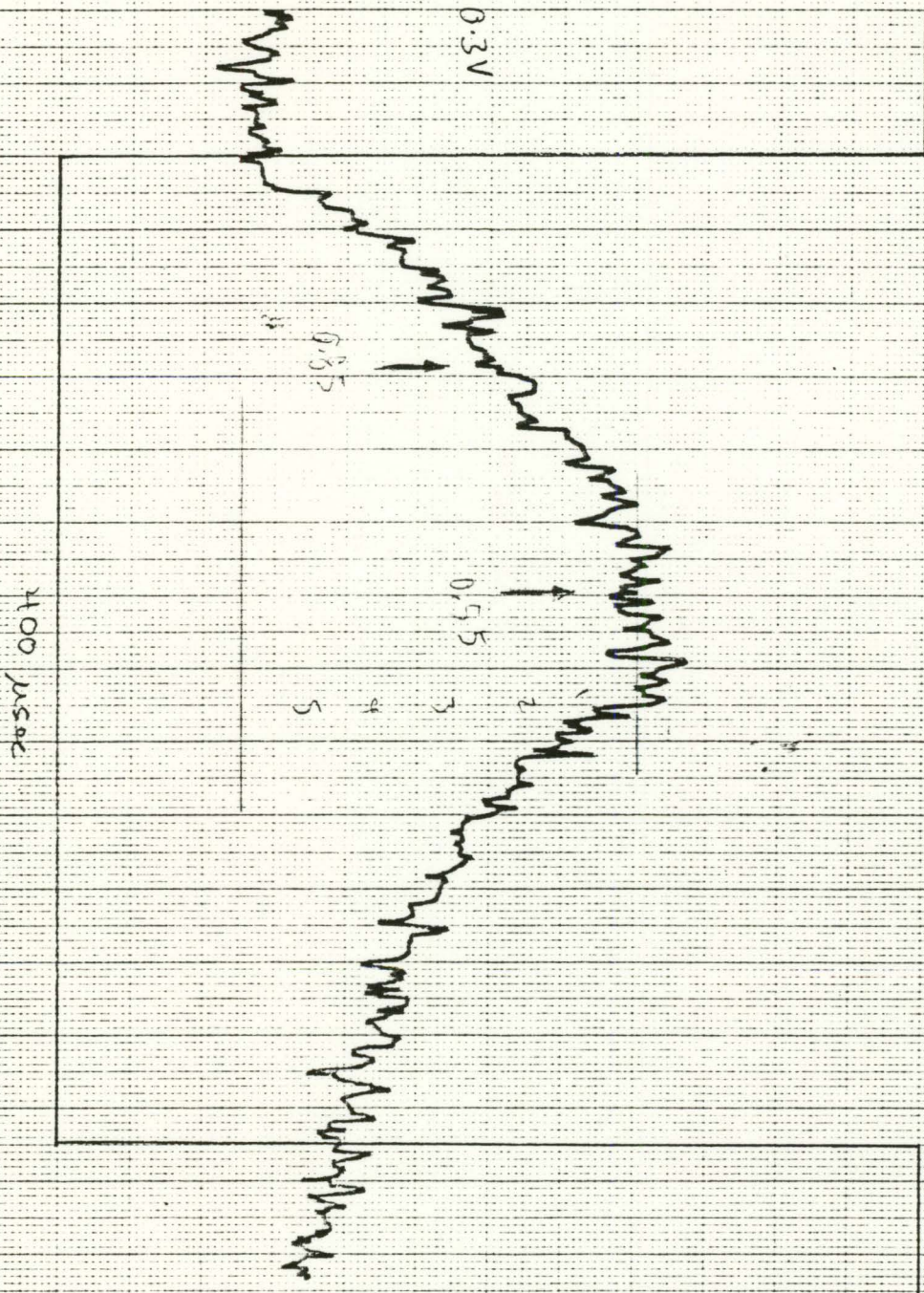
1600 INSEC

0.3 V



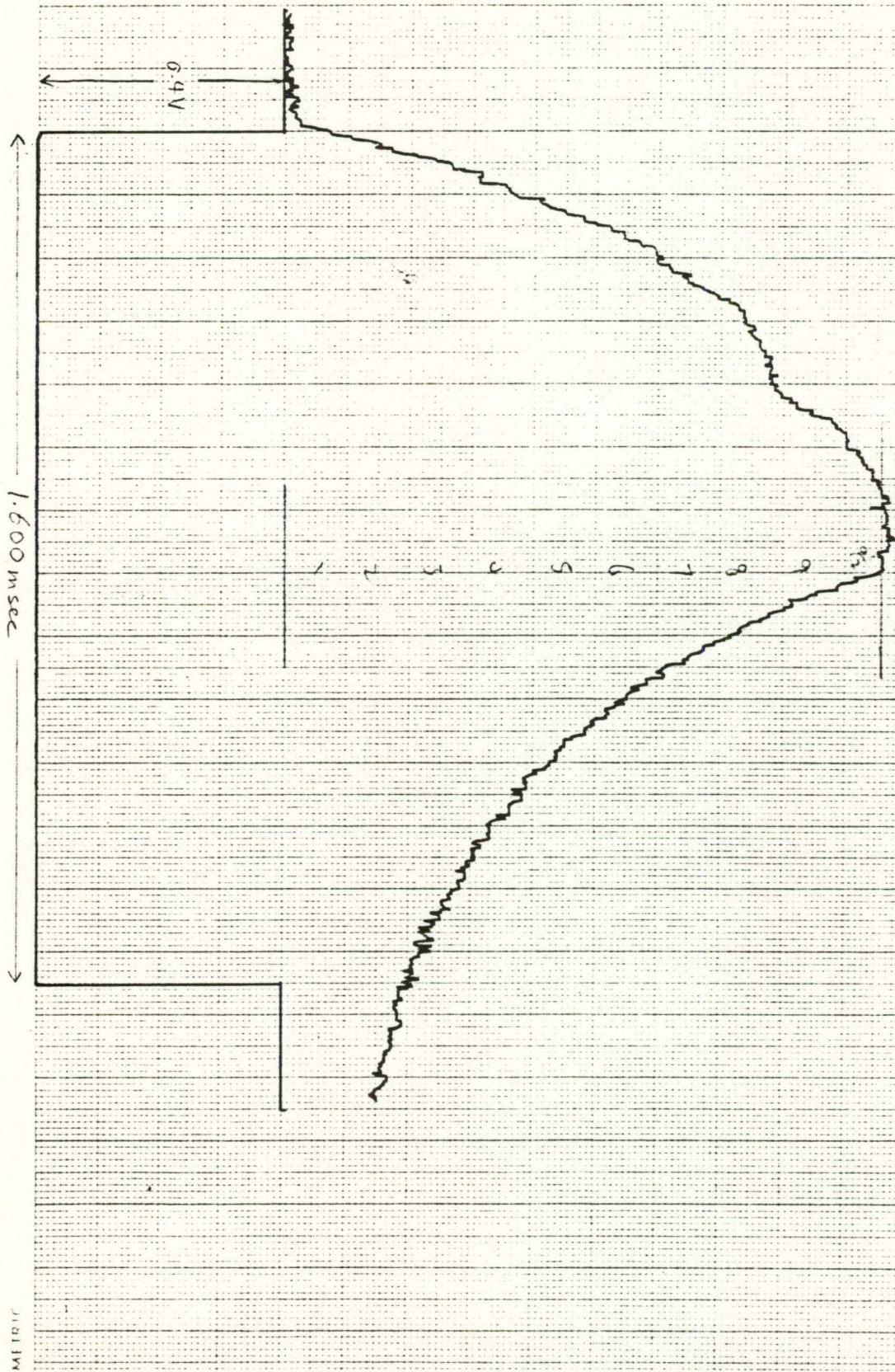


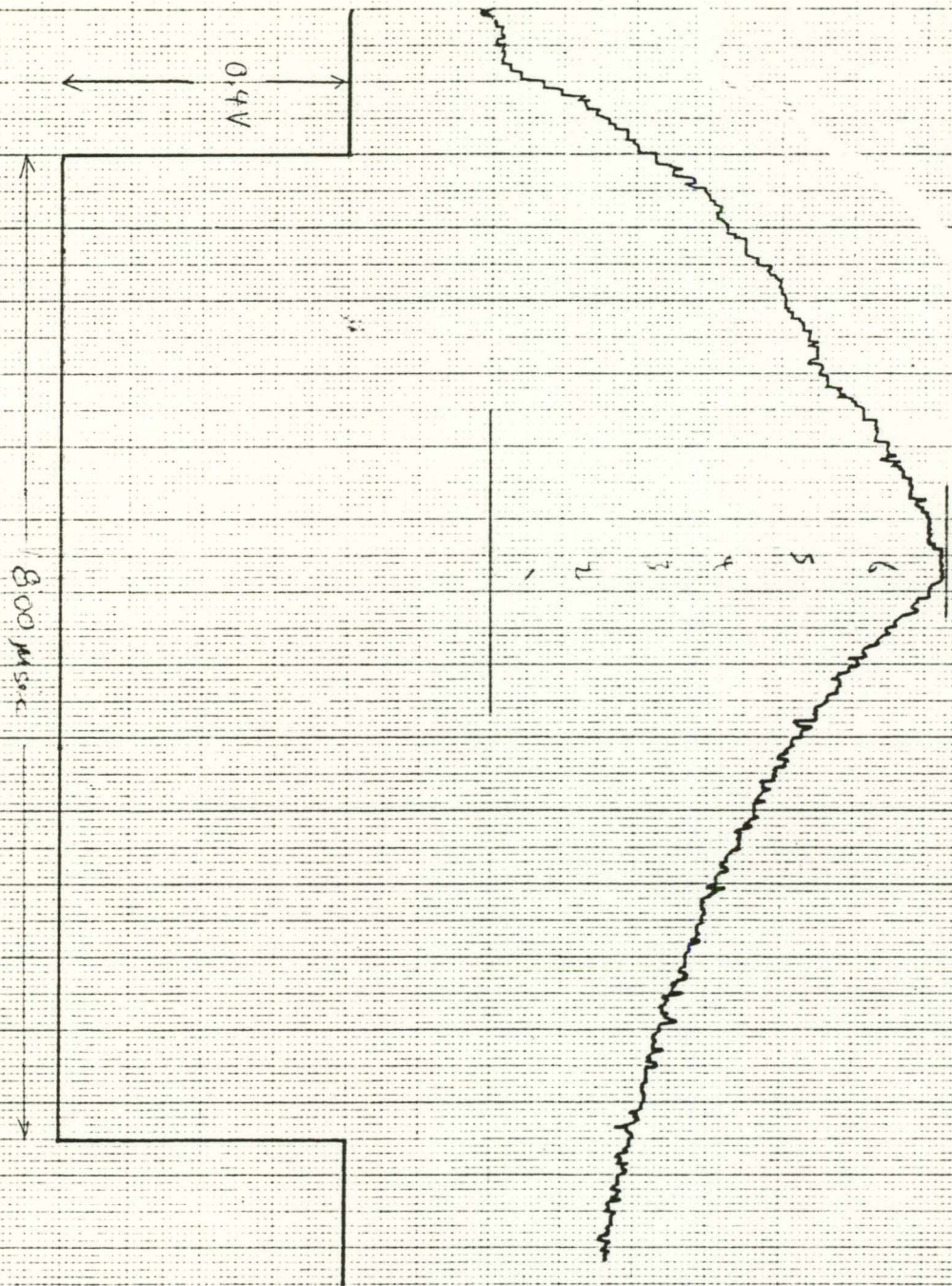
METRIC



@ 128 lines / sec

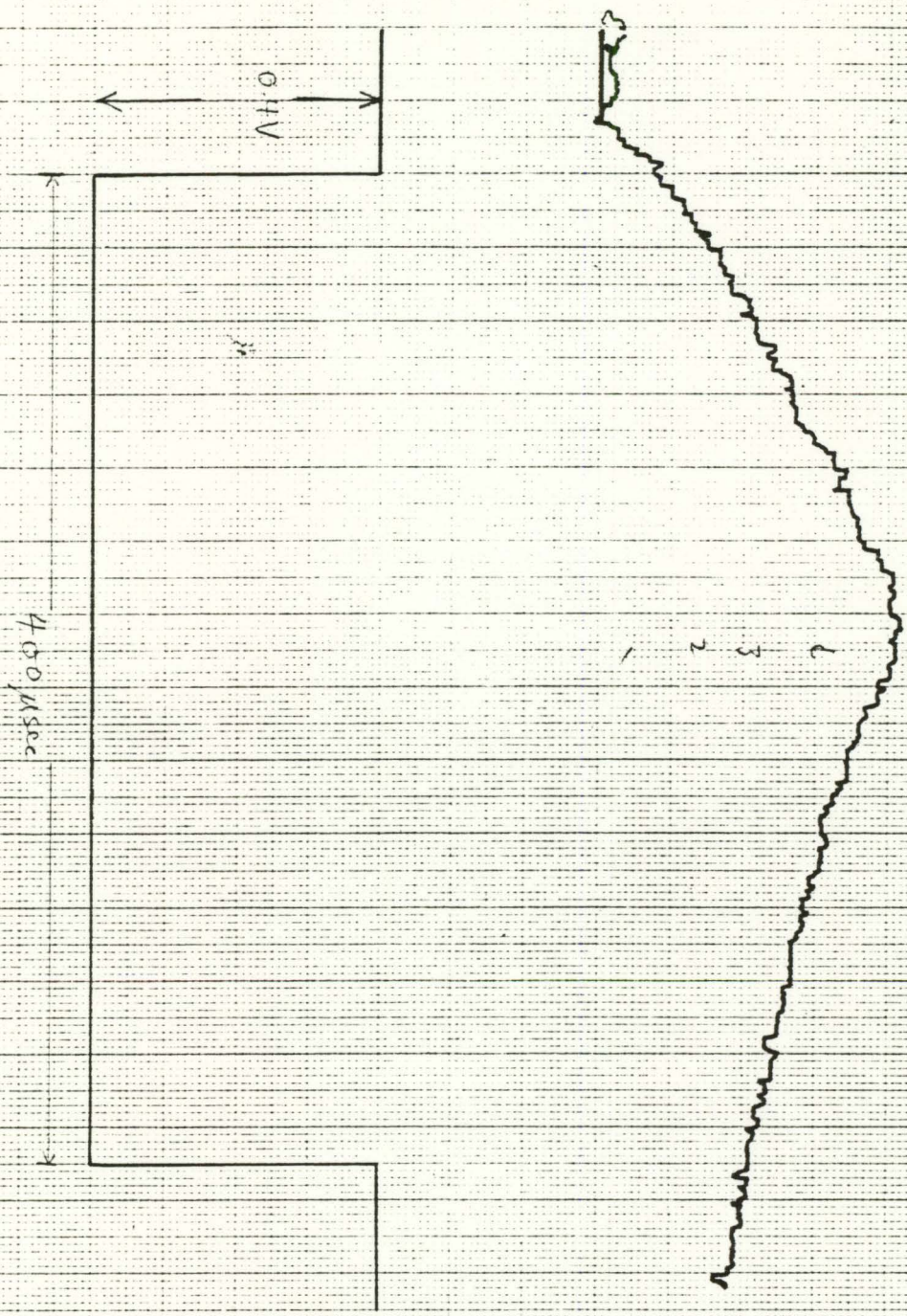
1114B





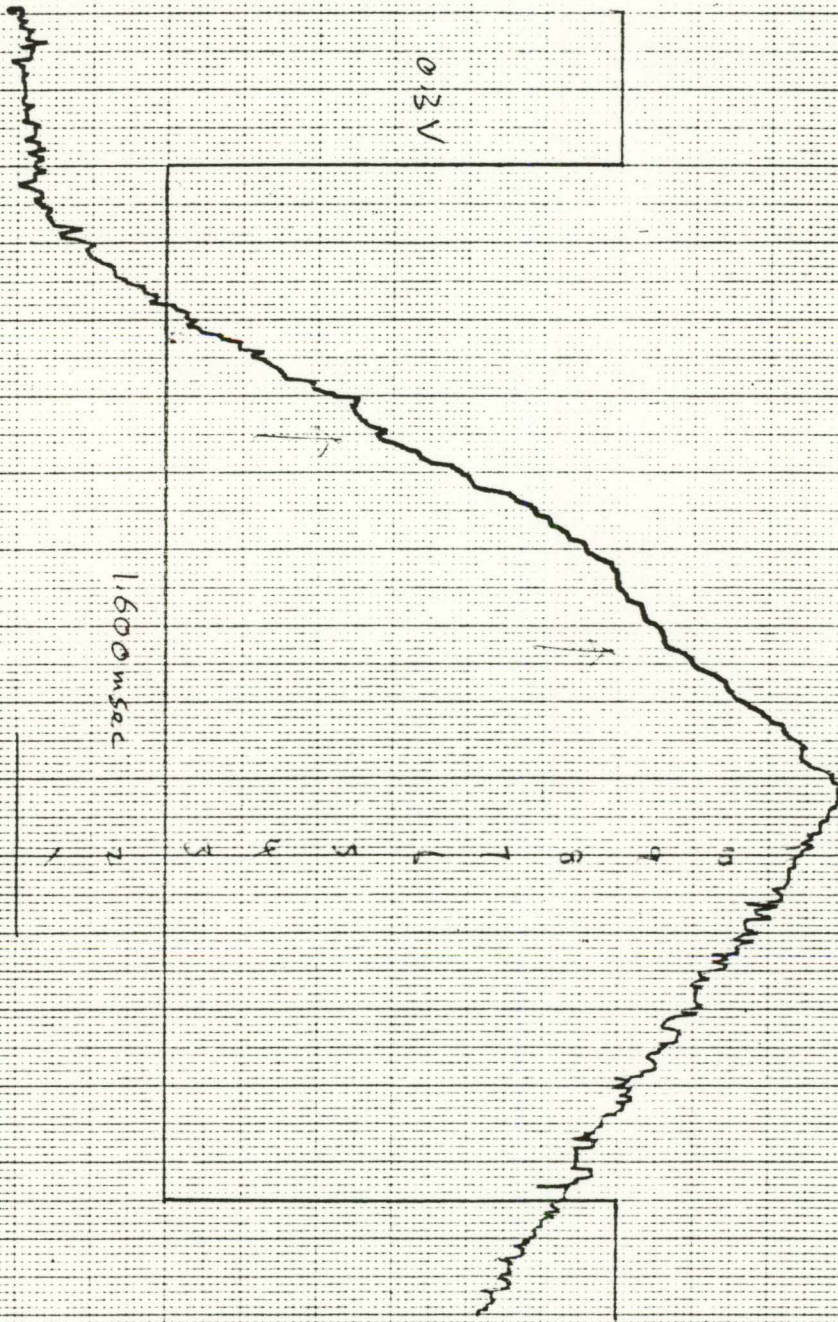
@ 512 lines/sec

* 1114B

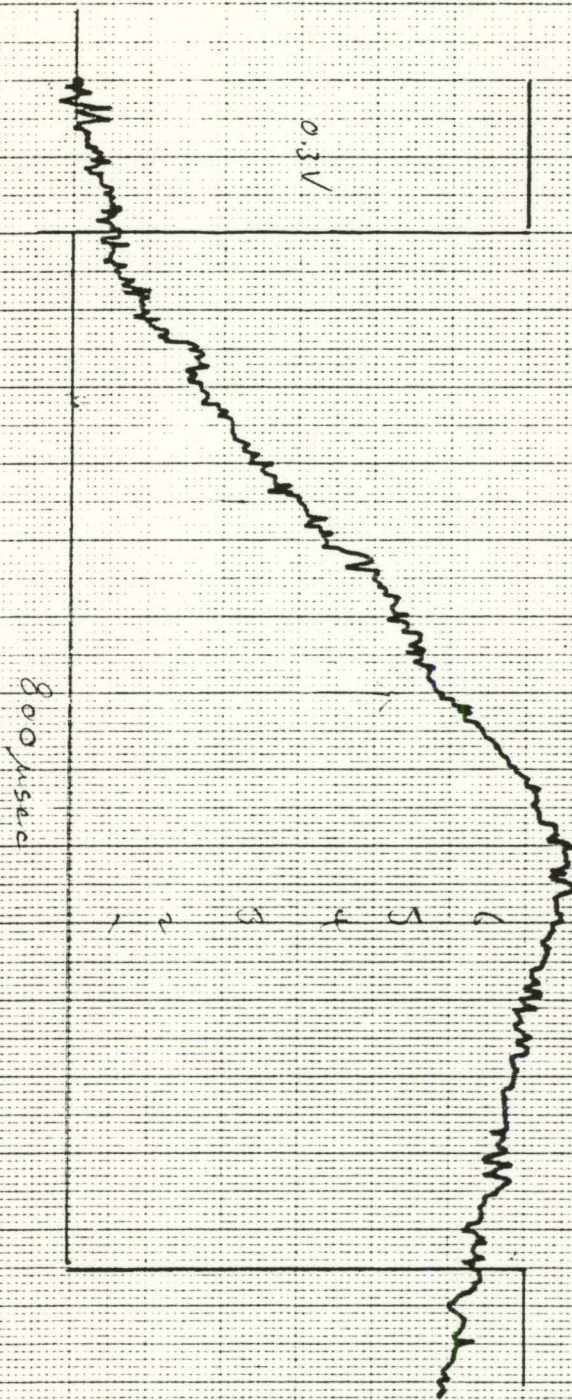


870A

@ 128 lines/sec



870 A @ 256 lines/sec



870 A @ 512 lines/sec

